

AN IMPROVED SPECTROSCOPIC ANALYSIS OF DA WHITE DWARFS FROM THE SLOAN DIGITAL SKY SURVEY DATA RELEASE 4

P.-E. Tremblay, P. Bergeron, and A. Gianninas

*Département de Physique, Université de Montréal, C.P. 6128, Succ. Centre-Ville,
Montréal, Québec H3C 3J7, Canada.*

tremblay@astro.umontreal.ca, bergeron@astro.umontreal.ca,
gianninas@astro.umontreal.ca

ABSTRACT

We present an improved spectroscopic and photometric analysis of hydrogen-line DA white dwarfs from the Sloan Digital Sky Survey Data Release 4 based on model atmospheres that include improved Stark broadening profiles with non-ideal gas effects. We also perform a careful visual inspection of all spectroscopic fits with high signal-to-noise ratios ($S/N > 12$) and present improved atmospheric parameters (T_{eff} and $\log g$) for each white dwarf. Through a comparison of spectroscopic and photometric temperatures, we report the discovery of 35 DA+DB/DC double degenerate candidates and 2 helium-rich DA stars. We also determine that a cutoff at $S/N = 15$ optimizes the size and quality of the sample for computing the mean mass of DA white dwarfs, for which we report a value of $0.613 M_{\odot}$. In the following step, we compare our results to previous analyses of the SDSS DR4 and find a good agreement if we account for the shift produced by the improved Stark profiles. Finally, the properties of DA white dwarfs in the SDSS are weighed against those of the Villanova White Dwarf Catalog sample of Gianninas et al. We find systematically lower masses (by about 3% on average), a difference that we trace back to the data reduction procedure of the SDSS. We conclude that a better understanding of these differences will be important to determine the absolute temperature scale and mean mass of DA white dwarfs.

Subject headings: white dwarfs – stars: atmospheres – stars: fundamental properties – stars: mass function

1. INTRODUCTION

The now completed Sloan Digital Sky Survey (SDSS; York et al. 2000) has rapidly grown to be, by far, the largest source of newly discovered white dwarfs in our galaxy. This project started as a survey of faint blue point sources and finally covered 9380 square degrees of the sky in the latest data release (Abazajian et al. 2009, Data Release 7). They mostly surveyed the North Galactic Cap region, with a completeness of about 95% for the point-source *ugriz* photometry. They performed a spectroscopic follow-up of nearly 1.6 million objects, mainly selected for their blue colors. White dwarfs from the different data releases have been identified in a series of papers (Harris et al. 2003; Kleinman et al. 2004; Harris et al. 2006), with the latest catalog published by Eisenstein et al. (2006) containing 9316 white dwarfs drawn from the Data Release 4 (the SDSS-E06 catalog hereafter), covering 4783 square degrees of the sky. The final catalog from the DR7 is currently in preparation (Kleinman et al. 2009) and will increase the total number of white dwarfs discovered in the SDSS by nearly a factor of two. While the SDSS survey has been the source of numerous discoveries of peculiar objects (this subject is too wide to review here), and even a new class of white dwarfs — the so called hot-DQ stars (Dufour et al. 2007), the most common class of objects — the hydrogen-line (DA) white dwarfs — has been at the center of only a few studies (Eisenstein et al. 2006; Kepler et al. 2007).

The largest published sample of spectroscopically identified DA white dwarfs can be found in the SDSS-E06 catalog. Considering the large number of SDSS spectra of all types, only the *most obvious* white dwarfs were recovered in this catalog. The main problem in the identification of white dwarfs in the SDSS is that at cool temperatures ($T_{\text{eff}} \lesssim 8000$ K), they overlap in a color-color diagram with A and F main-sequence stars. However, for hotter objects, they claim their catalog should recover most of the single DA stars observed spectroscopically by the SDSS. We will review their selection procedure in more detail in Section 2. The catalog provided individual atmospheric parameters — T_{eff} and $\log g$ — for each DA white dwarf, but this was not meant to be a careful analysis of these stars, especially given that many objects have been catalogued without a visual inspection. The only thorough follow-up analysis, so far, of the bulk of these white dwarfs has been reported by Kepler et al. (2007), who refitted more carefully all objects with $g < 19$, and concentrated in particular on the mass distribution, including a comparison with previous determinations from independent surveys, and a comparison of the mass distribution of DA stars with that obtained for the helium-line (DB) white dwarfs identified in the SDSS-E06. However, Kepler et al. did not provide any update of the atmospheric parameters (which differed from those published by Eisenstein et al.). DeGennaro et al. (2008) reviewed the luminosity function and completeness of the SDSS-E06 sample, but used the atmospheric parameters previously published by Eisenstein et al. In parallel, subclasses of the DA spectral type — e.g. magnetic

white dwarfs, DAO stars with detectable He II $\lambda 4686$, and the DA–M dwarf binaries — have been analyzed in various independent studies, covering partially, or in full, the SDSS-E06 catalog.

We have recently computed a new set of model atmospheres for DA white dwarfs, described in Section 2.2, which rely on the improved Stark broadening profiles developed by Tremblay & Bergeron (2009). These model spectra have already been applied to the hot white dwarfs in the Palomar-Green (PG) sample (Tremblay & Bergeron 2009), and they are also currently being applied to the large scale analysis of the DA stars in the Villanova White Dwarf Catalog¹ (Gianninas et al. 2009, 2011). In this paper, the same models are used in an independent analysis of the hydrogen-line (DA) stars identified in the SDSS-E06 catalog. In particular, we will obtain improved stellar parameters, which can be readily compared to those found in the PG sample and the Gianninas et al. sample based on the same model spectra and fitting technique. This will allow for a more robust test of the quality of the SDSS data reduction and sample selection.

The SDSS sample is unique in the sense that it includes many more objects than any other sample of white dwarfs previously compiled. This is certainly an advantage since it provides better statistics on rare peculiar objects. However, for the bulk of the regular DA stars, we can see in Figure 1 that the average signal-to-noise ratio (S/N) of the observed spectra is low, much lower than any other sample previously analyzed (see, e.g., Fig. 1 of Liebert et al. 2005). Therefore, we think it is essential to better quantify the reliability of lower S/N data, a point also raised by Koester et al. (2009). Kepler et al. (2007) used a simple magnitude cutoff, but here we propose a more detailed study of how the size of the sample can be optimized to yield average properties of the sample that have the most statistical significance. Finally, we have carried out a careful visual inspection of all the fits for objects with $S/N > 12$, a task that has not been accomplished until now, to our knowledge. In the course of this inspection, we have identified many new peculiar objects, misclassified in previous analyses, including a large number of degenerate binaries.

The goals outlined in the previous paragraphs led us to perform a complete and detailed follow-up of the studies of Eisenstein et al. and Kepler et al. by re-analyzing all DA white dwarfs in the SDSS-E06 sample. In Section 2, we summarize the set of SDSS observations and also describe our model atmospheres and fitting technique. We then present the results of our updated analysis in Section 3, where we define our optimal sample and also report the discovery of new degenerate binaries. Our results are compared in Section 4 with those of previous analyses of the SDSS-E06 sample as well as other samples of DA stars. Concluding

¹<http://www.astronomy.villanova.edu/WDCatalog/index.html>

remarks follow in Section 5.

2. DATA ANALYSIS

2.1. The SDSS Sample of DA White Dwarfs

The SDSS-E06 catalog relies on an automatic procedure to recover the white dwarf spectra in the survey. We briefly summarize this procedure in three main steps. A blue portion of the $g - r$ vs. $u - g$ diagram (see Fig. 1 of Eisenstein et al. 2006) is first defined to identify white dwarf candidates. As mentioned in the Introduction, white dwarfs cooler than ~ 8000 K occupy the same region as main-sequence stars in this two-color diagram, and most of them are therefore excluded by this first color cutoff. A second step is to eliminate candidates with a galaxy classification and a redshift larger than 0.003, although a few of them remain when a proper motion measurement is available with a value consistent with a nearby galactic source. Finally, the resulting photometric and spectroscopic observations for $\sim 13,000$ white dwarf candidates are compared to white dwarf models with a χ^2 minimization fitting technique. The outliers and objects with a poor fit are reclassified manually and in some cases rejected from the final catalog altogether. These steps seem quite robust in recovering all typical, hot, single DA white dwarfs. The authors of the catalog claim that it should be fairly complete for DA white dwarfs with $T_{\text{eff}} \gtrsim 8000$ K. However, they also remind us that the completeness of the SDSS spectroscopic survey itself can be anywhere between 15% and 50%, in part due to the neglect of blended point sources, as well as an incomplete spectroscopic follow-up of the point sources identified in the SDSS fields (Eisenstein et al. 2006; DeGennaro et al. 2008). For all other DA subtypes (e.g, magnetics, DA–M dwarf binaries, etc.), the picture is less clear. The most common subtype are the DA – M dwarf binaries where the presence of a cool main-sequence companion often changes the observed colors and contaminates the line profiles. The SDSS-E06 catalog is not tuned to identify systematically these objects. Other subtypes with spectra significantly different from that of a normal DA white dwarf, such as magnetics or DA stars diluted by a featureless DC companion, are also more likely to be rejected.

The basis of our analysis are the 8717 spectroscopic observations from the SDSS-E06 catalog with spectral type DA as the main classification, including some multiple spectra of the same objects. We obtained the spectroscopic and photometric observations from the SDSS Data Archive and Sky Server². The spectra, which cover a wavelength range of 3800

²das.sdss.org, cas.sdss.org

to $\sim 10,000 \text{ \AA}$ with a resolution of $R \sim 1800$, rely on the improved data reduction from the Data Release 7, where some data reduction problems observed in previous data releases have been corrected (Kleinman et al. 2009). We next computed the S/N for each object in the range from 4450 to 4750 \AA , a featureless spectral region between $H\beta$ and $H\gamma$, which provides a representative average for our spectroscopic technique. As expected, we can see in Figure 1 that the S/N of the spectra is closely correlated with the observed g magnitudes. We prefer to constrain the size of our sample based on S/N rather than magnitude because the former value is more directly related to the uncertainties in our fitting procedure described below. It is immediately clear that the faintest objects in the SDSS will not be included in the mean properties computation, because their atmospheric parameters carry large individual uncertainties. It also becomes increasingly difficult to identify DA subtypes (e.g. magnetics, DAB) when the noise level is high. For these reasons, we break the complete sample of DA spectra into two categories. The higher quality data (S/N > 12), for a total of 3249 stars (3550 different observations), are carefully analyzed through a visual inspection of each fit. The remaining lower quality data of the sample are fitted with automatic programs and used for reference only. Unless it is noted explicitly, all the numbers and figures in our analysis are based on the higher quality data only. The reason for the S/N = 12 cutoff is simply that a visual inspection of the lower quality spectra would not yield a significant number of interesting detections, and the publication of updated atmospheric parameters was deemed of low importance.

2.2. Model Atmospheres

For this work, we use the improved DA white dwarf model spectra that have been developed by our group in recent years. First of all, we rely on the Stark broadening tables of Tremblay & Bergeron (2009) with the non-ideal gas effects from Hummer & Mihalas (1988) included directly in the line profile calculations. Our models are similar to those used in their analysis in the range $40,000 \text{ K} > T_{\text{eff}} > 12,000 \text{ K}$, with the exception that we now add the non-ideal effects due to the electronic collisions in the equation of state as well (i.e., in addition to the line profiles). Tremblay & Bergeron (2009, see Sec. 2.3) argued that these effects could be neglected compared to proton perturbations, but we actually find that this physical ingredient still changes the mean properties by $\sim 1\%$. For cooler temperatures, we employ the same model grid as that described in Tremblay et al. (2010). In particular, we make use of the $ML2/\alpha = 0.8$ version of the mixing-length theory, which provides, within the context of our improved broadening profiles, the best overall internal consistency between optical and UV temperatures.

For the purpose of analyzing the hottest DA stars in the SDSS sample, we also computed new non-LTE model spectra with $T_{\text{eff}} > 40,000$ K using the publically available TLUSTY model atmosphere code and the accompanying spectral synthesis extension SYNSPEC (Hubeny & Lanz 1995). The only difference between this grid and that previously described in Liebert et al. (2005) is that we are now using our improved Stark broadening profiles, and the β_{crit} parameter was also set back to its original value (see Tremblay & Bergeron 2009 for details). It is worth mentioning that we include these new Stark profiles in both the atmospheric structure (TLUSTY) and model spectrum (SYNSPEC) calculations, while previous non-LTE grids calculated with TLUSTY relied on approximate analytical Stark profiles, based on the two-level approximation (similar to the assumptions of Lemke 1997), to compute the atmospheric structures. Because such analytical profiles could not be easily modified to take into account non-ideal effects, it was deemed necessary to replace these approximate profiles with our more detailed calculations. This improvement ensures that our Stark profiles are now included in a self-consistent way throughout all our calculations. Our complete grid of model atmospheres and spectra covers a range of $T_{\text{eff}} = 1500$ K to 140,000 K (by steps of 250 K for $T_{\text{eff}} < 5500$ K, 500 K for $6000 \text{ K} < T_{\text{eff}} < 17,000$ K, 5000 K for $20,000 \text{ K} < T_{\text{eff}} < 90,000$ K, and 10,000 K for $T_{\text{eff}} > 90,000$ K), with $\log g$ values from 6.0 to 10.0 (by steps of 0.5 dex with additional points at 7.75 and 8.25 dex).

2.3. Fitting Procedure

Our fitting procedure is similar to that outlined in detail in Liebert et al. (2005). Briefly, we first normalize the flux from the individual Balmer lines, in both the observed and predicted spectra, to a continuum set to unity. This continuum is defined by fitting the observed line profiles with a theoretical spectrum including a polynomial with several free parameters to account for residual errors in the flux calibration. We have slightly improved the method by using a larger wavelength range compared to previous analyses. In this first step, the models are not used in any way to infer the atmospheric parameters. This approach for normalizing the observed spectra is used for $T_{\text{eff}} > 16,000$ K and for $T_{\text{eff}} < 9000$ K, while at intermediate temperatures — where the Balmer lines reach their maximum strengths — we use several pseudo-Gaussians profiles, which constitute a more robust approach (Bergeron et al. 1995). Finally, the $\text{H}\alpha$ line is normalized independently from all other lines, using theoretical line profiles in all cases. We then proceed to a χ^2 minimization between the observed and predicted line profiles, convolved with a Gaussian instrumental profile with a resolution of 3 Å (FWHM) appropriate for the SDSS spectra.

Our atmospheric parameters determinations for the DA stars in the SDSS is meant to

be completely independent of previous analyses, other than the use of the DA designation from Eisenstein et al. (2006) for the main spectral type in the definition of our sample. It is well known that there is generally a cool and a hot solution for the fit to normalized Balmer lines, centered on the maximum strength of the hydrogen lines near $T_{\text{eff}} \sim 13,500$ K. In a first iteration, we determine the atmospheric parameters for each star assuming both a cool and a hot solution, and adopting as a preliminary solution that which provides the best agreement between the spectroscopic temperature (T_{spec}) and the photometric temperature (T_{phot} ; the photometric fits are described in Section 2.4).

The major improvement of our analysis is that we go through a second iteration for all stars with $S/N > 12$ and perform a careful visual inspection of each individual fit. While we only consider normalized Balmer line profiles to determine the atmospheric parameters, we also rely on two additional diagnostics to reclassify and to flag interesting objects. The first diagnostic is the dereddened *ugriz* photometry, which we fit with the same model fluxes. The second diagnostic is the direct comparison of the synthetic and observed absolute fluxes, assuming that the SDSS spectra are properly flux calibrated. Note that in the SDSS, the spectroscopic and photometric observations are independent. These two additional diagnostics are usually lacking in other large DA surveys, and this certainly represents a significant advantage of the SDSS sample. Our visual inspection revealed 52 confirmed magnetic white dwarfs, or magnetic candidates, and we remove these objects from our sample because these cannot be fitted, even approximately, with our non-magnetic models. We refer to the studies of Schmidt et al. (2003), Vanlandingham et al. (2005), and Külebi et al. (2009) for a more detailed analysis of these stars. We also remove 3 objects that are most likely not white dwarfs (J090917.09+002514.0, J204949.78+000547.3, and J205455.83+005129.7). The second object has actually been reobserved by Kilic et al. (2007) and confirmed as a non-degenerate. Finally we remove two DA stars for which the SDSS observations cannot be fit with our spectroscopic technique because more than two lines were unavailable or unusable.

The most common flag in our analysis is the presence of a red flux excess in 345 objects, generally with non-degenerate absorption lines, which in almost all cases reveals the presence of an M dwarf companion³. For 65 of these systems, there is an obvious contamination blueward of $H\beta$, and these are simply too difficult to analyze with our spectroscopic approach. For the remaining systems with a smaller contamination, we use a simple technique that has proven to be sufficient in the present context. We exclude one or two lines ($H\alpha$, $H\beta$) from the χ^2 fit, and in some cases the line cores when emission is present. We also carefully inspected

³We use the terminology of DA–M dwarf binaries throughout this work but it must be understood that some of them are merely candidates because the red excess is weak, and some companions are actually L dwarfs.

each fit, and were conservative in excluding all possibly contaminated lines. We find out that in most cases, the direct comparison of the synthetic and observed absolute fluxes is good in the region where the lines are fitted. We also use the $u - g$ color index to help in discriminating between the cool or hot solutions since the quality of the fit is generally a poor indicator due to possible contamination.

Even if the SDSS contains mostly faint white dwarfs (see, e.g., Fig. 1), there is still a large sample of high quality data — i.e. 665 spectra with $S/N > 30$, which is comparable in quality and quantity to other large surveys of DA stars (the PG survey for instance; Liebert et al. 2005). In Figure 2, we show sample fits from these high S/N observations. It is clear that by taking only the best spectroscopic data in the SDSS sample, one can still construct one of the best available sample of DA stars.

2.4. *ugriz* Photometry

In our overall fitting procedure, we also make use of *ugriz* photometric observations, which are available for most DA stars in the SDSS-E06 catalog. We fit the observed photometry of each object by using the grid of model atmospheres discussed in Section 2.2. We removed all individual magnitudes with a flag indicating that there might be a problem. Since the photometry is not sensitive to surface gravity, we simply assume the spectroscopic $\log g$ value and fit only the effective temperature T_{phot} and the solid angle $\pi(R/D)^2$, where R is the stellar radius and D is the distance from Earth. We apply a correction to the u , i , and z bands of -0.040 , $+0.015$ and $+0.030$, respectively, to account for the transformation from the SDSS to the AB magnitude system, as explained in Eisenstein et al. (2006). Finally, we deredden the photometry, in an iterative fashion, using the distance of the star found from the previous iteration, and the parameterization of Harris et al. (2006) for the amount of reddening as a function of distance⁴.

In the course of our inspection of the photometric and spectroscopic fits, we identified 37 double degenerates or helium-rich DA candidates that will be discussed in Section 3.4 and 3.5⁵ together with a more general comparison of spectroscopic and photometric temperatures. Note that we do not make any direct use of the photometric temperatures since these are

⁴We would like to point out here that interstellar absorption is assumed to be negligible for stars with distances < 100 pc, and that the absorption is maximum for stars with distances from the Galactic plane $|z| > 250$ pc. The absorption varies linearly along the line of sight between these distances.

⁵We also remove the double lined binary J125733.63+542850.5 identified by Badenes et al. (2009), and the magnetic DAH+DB system J084716.21+484220.3 first identified by Schmidt et al. (2003)

intrinsically less accurate, with larger internal uncertainties from the fitting procedure, and additional external uncertainties from interstellar reddening and photometric calibration.

3. RESULTS

3.1. Atmospheric Parameters

We present in Table 1 the atmospheric parameters for our final sample of 3072 DA stars with $S/N > 12$ whose fits were visually inspected. We exclude 161 objects, as discussed in the previous section, and we postpone the analysis of 16 DAO stars to Section 4.3. When multiple spectra of the same star are available in the DR4, we simply adopt the solution obtained with the highest signal-to-noise spectrum. We convert $\log g$ values into stellar masses using the evolutionary models with thick hydrogen layers of Fontaine et al. (2001) below $T_{\text{eff}} < 30,000$ K and of Wood (1995) above this temperature; we also provide in Table 1 the corresponding white dwarf cooling time ($\log \tau$). Low-mass white dwarfs, below $0.46 M_{\odot}$ and $T_{\text{eff}} < 50,000$ K, are likely helium core white dwarfs, and we rely instead on evolutionary models from Althaus et al. (2001). For masses higher than $1.3 M_{\odot}$, we use the zero temperature calculations of Hamada & Salpeter (1961). The absolute visual magnitude M_V obtained from spectroscopic measurements of T_{eff} and $\log g$ is also given for each object following the calibration of Holberg & Bergeron (2006).

The errors of the atmospheric parameters given in Table 1 are the *internal* uncertainties of our fitting procedure, which are correlated to the S/N (see, e.g., Bergeron et al. 1992). The true error budget also needs to take into account the *external* uncertainties from the data calibration. There are 301 repeated observations for stars in Table 1 that can be used to quantify the external errors. These alternative observations, in general with S/N only slightly lower than the primary observation, were fitted and visually inspected with our standard procedure. In Table 2, we compare the internal and external errors for these multiple observations. A similar procedure has been used by Eisenstein et al. (2006), but since uncertainties are expected to be a function of both T_{eff} and S/N , here we break the sample into various bins for each quantity. We find that external uncertainties are always very similar to the internal uncertainties. This confirms the consistency of the data acquisition and pipeline reduction procedure of the SDSS spectra. We note that our comparison cannot reveal systematic reduction problems, however, and such effects will be discussed in Section 4.2 from a comparison with independent observations.

In Figure 3, we present the mass distribution as a function of effective temperature for our sample of DA stars. As we want to illustrate the effect of the quality of the observations

on this distribution, we show in the upper panel the results with the higher quality spectra ($S/N > 20$) and in the bottom panel with the lower quality spectra ($20 > S/N > 12$); each subsample has a roughly equal number of stars. For clarity, we postpone the discussion of the hottest stars ($T_{\text{eff}} > 40,000$ K) to Section 4.3. Below $T_{\text{eff}} \sim 13,000$ K, we observe the well-known increase in the mean mass, the so-called high- $\log g$ problem discussed at length in Tremblay et al. (2010) and references therein. The bottom panel indicates that the mass distribution obtained with lower S/N data is similar to that with higher quality spectra in the intermediate range of effective temperature where the hydrogen lines are particularly strong ($30,000 \text{ K} > T_{\text{eff}} > 10,000 \text{ K}$). However, larger spreads in the mass distribution can be seen at the high and low temperature limits of our sample, in a region where hydrogen lines become weaker and more sensitive to the quality of the observations. Furthermore, since the flux in the blue portion of the spectrum is intrinsically less important in cooler stars, the S/N also becomes much smaller below 4000 \AA — a region sensitive to $\log g$ — than at longer wavelengths, and the atmospheric parameters of cooler stars are thus expected to become less accurate. An examination of our error budget in Table 2 indeed confirms that at cool temperatures and low S/N, the external error of $\log g$ is indeed roughly twice that of the average of the sample.

As already mentioned, one of the most important aspects of our analysis is the careful visual inspection of each individual fit. In Figures 4 and 5 we show illustrative examples for three objects. We specifically look at the following diagnostics: (1) the quality of the spectroscopic fit (left panels), (2) the quality of the photometric fit (right panels), (3) the comparison of the spectroscopic and photometric temperatures, (4) the superposition of the observed photometry and fluxed spectra, and finally (5) the superposition of the model fluxes normalized at r and calculated at the spectroscopic values of T_{eff} and $\log g$. On the top panels of Figure 4 is an example of a case with an excellent internal consistency between model and spectroscopic/photometric observations, a situation we observe for about 95% of single DA stars. On the bottom panels of Figure 4 is an example of a problem we encounter in about 5% of the stars in our sample (although, generally, to a lesser extent than what is shown here). In these situations, the slope of the observed spectrum disagrees with that inferred from photometric colors. This occurs more often for the reddest and coolest white dwarfs in the sample. In most cases, all other aspects of the visual inspection are as expected (i.e., a good spectroscopic fit, and a good agreement between spectroscopic and photometric temperatures). This clearly suggests that errors in the flux calibration are the most likely explanation for this discrepancy. The observed spectrum of J003511.63+001150.3 shown in Figure 4 is actually a repeated observation; a primary spectrum with a slightly higher S/N was used to determine the atmospheric parameters given in Table 1. The primary spectrum is actually in agreement with the photometric colors, confirming the hypothesis

that a fraction of SDSS spectra may have an erroneous flux calibration. Kleinman et al. (2004) claim that the SDSS spectra are spectrophotometrically calibrated to within about 10%, on average, so some discrepancy, such as that shown in Figure 4, should not be totally unexpected. The trend we observe, however, is that the flux calibration is good to within a few percent for most objects, but is significantly worse for a minority ($\sim 5\%$) of cases. We added a note in Table 1 (see Note 2) to flag these particular observations, but these objects should not be considered as peculiar white dwarfs. On the other hand, there are a few cases (about 1%) where the predicted energy distribution inferred from the spectroscopic solution disagrees with both the slope of the observed spectrum *and* the photometric colors, as illustrated on the top panel of Figure 5. In other words, there is a poor match between T_{spec} and T_{phot} , even though the spectroscopic fit appears normal. We note that one could also select the cool spectroscopic solution for this object, to obtain a better match with the photometric temperature. This case is displayed on the bottom panel of Figure 5, and while the agreement between T_{spec} and T_{phot} is better, the Balmer line profiles are clearly at odds with the model predictions. Objects similar to those shown here are believed to be genuine peculiar stars and these are further discussed in Sections 3.3 and 3.4.

3.2. Mass distribution

In this section, we attempt to best characterize the mass distribution of DA stars using the SDSS-E06 sample. We restrict our analysis to stars cooler than $T_{\text{eff}} = 40,000$ K due to possible systematic effects from metal contaminations (see Section 4.3), and to stars hotter than 13,000 K because of the high- $\log g$ problem discussed above. We also eliminate, for the time being, all DA–M dwarf binaries; these will be discussed further in Section 4.4. As a first step, we look for a compromise between the quality of the spectra and the size of the sample, as discussed in the Introduction. We saw in the preceding section that we could obtain sound results using all stars with $S/N > 12$, but we should be cautious at the hot and cool ends of the distribution.

To make a more quantitative assessment of the optimal sample for computing the mass distribution, we break our sample into S/N bins containing a nearly equal number of stars. In Figure 6, we present the mean mass and standard deviation as a function of S/N ⁶. In the ideal case of a homogeneous spectroscopic data reduction as a function of S/N , the mean

⁶For $S/N < 12$, we used an automatic fitting procedure similar to that employed for the higher quality spectra. In order to get a relatively clean sample, we removed DA–M dwarf composite systems using color criteria and all other outliers that did not fall within the range of $6.5 < \log g < 9.5$

mass should be constant over the whole sample. The standard deviation, however, should be close to the intrinsic value of the underlying mass distribution at high S/N, but should increase when the errors of the individual mass measurements become significant compared to the true dispersion of the sample. We can see in the upper panel of Figure 6 that the mean mass remains fairly constant, even down to very low S/N values ($S/N \sim 8$), which implies that as a whole, we can trust the SDSS spectroscopic data in this range of S/N. The standard deviation, displayed in the bottom panel of Figure 6, appears as a more efficient means of selecting an appropriate S/N cutoff. It shows clearly that for low S/N, the large individual uncertainties in the mass measurements alter significantly the mass dispersion. We conclude that a cutoff at $S/N = 15$ is a good compromise to obtain the best statistical significance, that is, a large sample with sufficiently accurate spectroscopic measurements. As can be seen from Figure 1, this cutoff corresponds to a $g \sim 19$ cutoff, similar to the value used by Kepler et al. (2007) and DeGennaro et al. (2008) based on analogous arguments.

In Figure 7, we show our final mass distribution for the DR4 sample ($40,000 \text{ K} > T_{\text{eff}} > 13,000 \text{ K}$), which yields a mean mass of $\langle M \rangle = 0.613 M_{\odot}$. We note the presence of an excess of low-mass objects and a high-mass tail, which are qualitatively similar to those reported by Kepler et al. (2007) in their analysis of the same sample. We also demonstrate in this plot that the adoption of a slightly larger S/N cutoff of 20, rather than 15, does not change significantly the mean properties, or even the shape, of the mass distribution. While it is obviously much more difficult to identify subtypes (i.e., magnetics, DAZ, DAO, etc.) or to pinpoint the exact boundaries of the ZZ Ceti instability strip (Gianninas et al. 2005), the atmospheric parameters of normal DA white dwarfs appear reasonable down to low S/N, with admittedly increasing uncertainties.

3.3. Comparison of Spectroscopic and Photometric Temperatures

The comparison of our spectroscopic and photometric effective temperatures is displayed in Figure 8. For clarity, we only show the results for DA spectra with $S/N > 20$; the comparison with lower S/N data is similar, with a slightly higher dispersion. Since the photometry becomes increasingly insensitive to effective temperature at the hot end of the sample, we do not consider objects with both T_{spec} and T_{phot} over 40,000 K. We find that the agreement is generally good, with a small standard deviation of $\sim 8\%$, although some outliers are also clearly present. More importantly, there is a significant offset, with the spectroscopic temperatures being higher than the photometric temperatures by $\sim 4\%$, on average. There could be different explanations for this discrepancy, which we discuss in turn.

One important uncertainty is the dereddening procedure, which has an effect even for

the brightest stars in the sample. The procedure used here, taken from Harris et al. (2006), seems realistic in terms of the galactic structure, but the ratio of the actual to the full galactic reddening along the line of sight is uncertain by at least a few percent, due to the simplicity of the parameterization. The offset in Figure 8 increases to $\sim 6\%$ if we do not apply any reddening correction to the photometry; conversely, a large and unrealistic extinction, close to the maximum value, is necessary to remove the offset at $T_{\text{eff}} \sim 20,000$ K. The reddening uncertainty is therefore not large enough to be the main source of the observed offset. The second possible explanation for the offset is related to the photometric system transformations discussed in Section 2.4. Since these corrections are based on older models and data reductions (from Data Release 4), they might have to be revisited, although Eisenstein et al. (2006) quote uncertainties of the order of 1%, smaller than the discrepancy observed here. Furthermore, we verified that, on average, the observed and predicted photometry are in agreement within less than 0.01 magnitudes for all filters.

A third source of error might be related to a problem with the spectroscopic temperatures. It is shown later in this work (Section 4.2) that the spectroscopic temperatures obtained using SDSS spectra are on average 2% higher (for $T_{\text{eff}} > 13,000$ K) than those obtained using data from Gianninas et al. (2011) for objects in common. This discrepancy, likely due to systematic data reduction problems, could easily explain half of the offset observed in Figure 8. A fourth possible source of uncertainty is that we cannot claim to be more accurate than 1% in terms of the physics of the models, and therefore on the absolute scale of the spectroscopic temperatures. However, we can at least claim that our improved models yield absolute visual magnitude measurements, derived from spectroscopic values of T_{eff} and $\log g$, that are consistent with those derived from trigonometric parallax measurements (see Fig. 14 of Tremblay & Bergeron 2009). Finally, another option would be that the offset is real, at least for some objects. In the next section, we demonstrate that unresolved DA+DA binaries may indeed cause a systematic positive offset between spectroscopic and photometric temperatures.

We conclude that each of the uncertainties discussed above are able to explain about half of the observed offset, and there is thus no easy way to interpret the absolute spectroscopic and photometric temperature scales of white dwarfs at this point. Until these issues are resolved, the photometric temperature scale should not be discarded too easily, even if the internal uncertainties are larger.

Finally, we find in the comparison of spectroscopic and photometric temperatures displayed in Figure 8 a small number of outliers. A closer inspection of all objects with a 2σ discrepancy reveals that some of these outliers (red circles in Fig. 8) have already been flagged in Table 1 as being problematic due to poor spectrophotometry or glitches in the

observed spectra. These objects are thus unlikely to be real peculiar white dwarfs. However, many other outliers exhibit He I lines in their spectra and/or have poor fits. This suggests that these objects most likely represent DA+DB or DA+DC unresolved degenerate binaries. We analyze these systems further in the following section.

3.4. Double Degenerate Binaries

To better understand, from an observational point of view, how double degenerate binaries can be detected in the SDSS, we first present a simulation performed using a set of synthetic models. Since we are mostly interested here in the DA stars found in the SDSS, we simulate double degenerate systems containing at least a DA star together with another white dwarf of the DA, DB, or helium-rich DC spectral type. Individual model fluxes are thus combined for each assumed component of the system, properly averaged by their respective radius, to which we add a Gaussian noise of $S/N = 30$; synthetic *ugriz* photometry is also extracted from the resulting spectrum. The simulated data are then analyzed with our standard fitting procedure under the assumption of single DA star models. For the sake of simplicity, all calculations are made for a sequence of T_{eff} from 6000 to 40,000 K with steps of 2000 K for both components of the system. We computed all possible combinations in this range of temperatures with equal values of $\log g = 8$ for both components, as well as with a $\log g$ difference of 0.5 dex ($\log g = 7.75$ and 8.25 to be explicit). The results of this experiment are presented in Figure 9 where we compare spectroscopic and photometric effective temperatures; open circles represent DA+DA binaries, while filled circles correspond to DA+DB/DC binaries.

An examination of our results first reveals that all DA+DA binaries are indistinguishable from single DA stars in this diagram. Therefore, one absolutely needs additional constraints, such as trigonometric parallax or radial velocity measurements, to identify DA+DA binaries in the SDSS. Liebert et al. (1991) have already shown that combining the model spectra of two DA white dwarfs results, in general, in an apparently normal object that can be fitted successfully with single star models. What we find here is that the combined *ugriz* photometry can also be fitted with single star models, and that the photometric temperature happens to be within $\sim 10\%$ of the spectroscopic solution, even if the two DA components of the system have large temperature differences. Figure 9 also reveals that the spectroscopic temperatures are systematically larger than the photometric temperatures for DA+DA composites. A careful examination of this puzzling result reveals that the offset is due to the fact that the average spectroscopic temperatures just happen to be systematically larger than the average photometric temperatures. Since the observed offset in Figure 8 is of exactly the

same order as that simulated in Figure 9, it is of course tantalizing to suggest that most DA stars might actually be DA+DA composite systems! But we will refrain from doing so since, coincidentally, various systematic uncertainties in the spectroscopic and photometric temperature determinations are expected to produce similar offsets, as discussed in the previous section.

The situation is very different for the DA+DB/DC binary simulations shown in Figure 9, for which a large number of outliers can be easily identified. The spectroscopic fit of these objects would also often be flagged due to the presence of He I lines and a poor fit of the lower Balmer lines (typically the depth of H α is too shallow compared to a single star model). Even when the temperature of the DB/DC component is only half that of the DA component ($T_{\text{eff-DB/DC}}/T_{\text{eff-DA}} = 0.5$), these objects still appear as outliers in Figure 9 since the $\sim 5\%$ additional continuum flux is still important in the core of the deep Balmer lines. For lower values of $T_{\text{eff-DB/DC}}/T_{\text{eff-DA}}$, it becomes almost impossible to confirm the presence of a companion, unless the He-rich component shows strong He I lines and the S/N is particularly high.

In light of these results, we refined our criteria to find all DA+DB/DC in our sample by specifically searching for He I lines, but found only one additional star⁷ that was not in the $> 2\sigma$ outlier region in Figure 8. In our simulation of double degenerates, we also find a temperature regime ($T_{\text{spec}} \sim 10,000$ K in Fig. 9) where we obtain a good match between photometric and spectroscopic temperatures, yet the spectroscopic fit is poor at H α (and possibly additional low Balmer lines). One example of such a system is shown at the bottom of Figure 5, where H α (and to a lesser extent H β and H γ) is clearly at odds with the model predictions, and appears *diluted* by a companion. Six double degenerate candidates were identified in this manner from our DA sample.

We now proceed to fit all our double degenerate candidates with appropriate model spectra; our grid of DB models is described, for instance, in Limoges & Bergeron (2010) and references therein. We use an alternative version of our fitting program described above to extract the normalized hydrogen and helium (if present) line profiles of all candidates. Then a χ^2 minimization is performed between the observations and our set of DA and DB/DC models, with the T_{eff} and $\log g$ of each component of the system considered a free parameter. We assume that all objects are physical binaries, i.e. at the same distance, and therefore the flux ratio between the components is fixed by the set of atmospheric parameters.

We find in our sample a total of 35 binary candidates, including 10 DA+DB and 25 DA+DC systems. The fits are displayed in Figures 10 and 11, and the corresponding atmo-

⁷We exclude here hot DAO stars with $T_{\text{eff}} > 40,000$ K.

spheric parameters are reported in Table 3 along with additional comments for each system. For all DA+DC candidates, it is not possible to fit all four parameters since the dilution effects produced by a more massive (smaller radius) DC component are qualitatively comparable to those of a cooler object. Therefore, we simply assume a value of $\log g = 8$ for all DC stars. Furthermore, we observe that when the S/N is low, or when the hottest object is a DB/DC star, it is difficult to constrain the $\log g$ value of any component; in these cases a value of $\log g = 8$ is assumed for both stars. We find that, in general, the errors of the atmospheric parameters are significantly larger than those obtained for single stars. This is a direct consequence of considering two additional free parameters in our fitting procedure, and also results from the weakness of some of the observed spectral features.

We also compared for all binary candidates the predicted and observed *ugriz* photometry. We show an example for DA+DB and DA+DC systems in Figure 12. Here we calculate the predicted *ugriz* photometry with the atmospheric parameters given in Table 3, and simply match it to the observed photometry using a single scaling factor. We thus make no attempt to actually fit the observed photometry since there would be too many free parameters in our fitting procedure. In general, we find that this straightforward comparison between predicted and observed photometry yields an acceptable match, which is better or similar to that obtained under the assumption of a single star model, with the exception of a few objects identified in Table 3. We note that, unlike single stars, the predicted photometry is sensitive to the surface gravity of both stars since the relative contribution of each component of the system to the total flux — and thus the shape of the energy distribution — depends on their respective stellar radius. Therefore we do not put too much emphasis on small discrepancies, especially when the $\log g$ values are assumed in the spectroscopic fits.

All 35 binary systems listed in Table 3 represent new discoveries, with the exception of J034229.97+002417.6 (also known as KUV 03399+0015) first identified as a DA+DB system by Limoges & Bergeron (2010) as part of their spectroscopic analysis of the white dwarfs found in the Kiso survey. Our findings suggest that $\sim 1\%$ of all white dwarfs are in compact DA+DB/DC double degenerate systems. We note, however, that a binary system containing a fairly hot DB component is likely to be classified as a DBA star in the DR4, and not be included in our analysis. The mean $\log g$ value for the 20 DA components for which the surface gravity could be constrained is $\langle \log g \rangle = 8.12$. Since most of these DA stars are in the range of effective temperature where the high- $\log g$ problem is observed ($T_{\text{eff}} \lesssim 13,000$ K), this average value thus appears entirely consistent with that of single DA stars. The mean surface gravity for the 10 DB components is $\langle \log g \rangle = 8.21$, a value significantly larger than that of DA stars. This is perhaps not surprising since DB stars with $T_{\text{eff}} \lesssim 15,000$ K (7 out of 10 DB components in Table 3) have a tendency to have spectroscopic $\log g$ values larger than average (see, e.g., Beauchamp et al. 1996; Kepler et al. 2007).

We have also considered the alternative possibility that our composite systems are single DAB stars. By computing a grid of DAB model spectra with a homogeneous composition, and using the same physics as that discussed above for the DA and DB models, we find that in all but one case, the spectroscopic and photometric fits are less satisfactory than for the DA+DB composite fits. This is not surprising since for a DAB star, we expect a good match between T_{phot} and T_{spec} , similar to a single DA star, but most of our DA+DB binary candidates appear as outliers in Figure 8. The only object for which we could not clearly distinguish between a DA+DB and a DAB solution is J015221.12–003037.3, displayed in Figure 13.

For a few additional objects (see, e.g., J084742.22+000647.6, J084958.32+093847.7 and J093432.66+065848.6), the core of the lower Balmer lines (especially $H\alpha$ and $H\beta$) is poorly reproduced by the models, despite a good overall spectroscopic fit and a decent match to the observed photometry. One possible solution to this problem is that the DB component might actually be a DBA star. The DBA subtype is common enough to suggest that a few of them should be hiding in our sample, and at least one DA+DBA composite system has previously been identified in the MCT survey (Wesemael et al. 1994). Due to higher atmospheric pressures in DBA stars compared to DA stars, the hydrogen lines will be more quenched, or in other words, $H\alpha$ and $H\beta$ are expected to be much stronger than the higher Balmer lines. Hence, a DA+DBA composite system will first be identified from unusually large equivalent widths of the lower Balmer lines. We confirm, in Figure 14, that the use of a grid of DBA models (with fixed $H/He = 10^{-3}$ abundances) can slightly improve the quality of the spectroscopic fits for the three objects mentioned above. The addition of a free parameter — the hydrogen abundance in the DBA star — could be used to improve the fits. However, it is not easy to constrain, and we postpone any determination of this parameter until independent, higher S/N observations are secured.

We find that cool, weakly magnetic white dwarfs, especially at low S/N, often resemble DA+DC degenerate binaries since their lines appear broader and weaker compared to non-magnetic DA stars. The photometric fits of these magnetic stars are generally good, but a discrepancy between the photometric and spectroscopic temperatures is also present, obviously due to the fact that our non-magnetic models fail to reproduce the observed spectrum. The presence of Zeeman-split line cores can, in such cases, confirm the magnetic interpretation. However, there is one published magnetic star candidate (J231951.72+010909.0; Vanlandingham et al. 2005) which could easily fool our fitting procedure, since the Zeeman splitting is not apparent, and the *diluted* Balmer lines can be fitted almost perfectly with a DA+DC composite, although with a poor photometric match. We have thus been cautious to inspect every object that was initially flagged as a possible DA+DC composite, and were able to eliminate six DA stars that are more likely to be weakly magnetic stars rather than binaries

(J075842.68+365731.6, J132340.34+003338.7, J133007.57+104830.5, J144244.18+002714.8, J150856.93+013557.0 and J224444.62+130521.5). All these objects indeed show hints of triple or enlarged cores, and good photometric fits can be achieved with single star models. We also identify nine DA+DC candidates in Table 3, where the presence of a weak magnetic field remains a valid option. In conclusion, it is now clear that better S/N observations are needed to properly identify DA+DC candidates.

Many binary candidates in our sample show very weak hydrogen lines superposed on an otherwise flat spectrum, where the DC star is obviously the hotter and more luminous component of the system. These objects could alternatively be interpreted as single helium-rich DA stars with only small traces of hydrogen in their atmospheres. In principle, however, such stars could be differentiated from degenerate binaries since the hydrogen lines in a helium-dominated atmosphere would be heavily quenched by the high photospheric pressure, with only $H\alpha$ and $H\beta$ visible in their spectrum. In contrast, most hydrogen lines in the Balmer series will be detectable in the spectrum of a lower pressure $T_{\text{eff}} \sim 7000$ K DA atmosphere, diluted by a $T_{\text{eff}} \sim 10,000$ K DC⁸. Unfortunately, both scenarios predict hydrogen lines that are extremely weak and difficult to detect unambiguously at low S/N. We attempted to fit all our binary candidates with a grid of mixed hydrogen and helium models and we find that in eight cases, the fits are equally as good as the binary fits. The reason is that the S/N is too low to detect the higher Balmer lines even if they were present.

To conclude this section, we are fairly confident that we have correctly identified nine DA+DB degenerate binaries in the SDSS-E06 sample, since the quality of the fits as well as the comparison between the observed and predicted photometry clearly rules out the possibility of a single DAB star. The picture is less obvious for our DA+DC binary candidates (and one possible DAB star) but we are still confident that most of the candidates listed in Table 3 are indeed degenerate binaries. Further monitoring of these stars, such as radial velocity measurements, will be required to confirm their binary nature. Incidentally, all SDSS spectra are in fact taken in three or more exposures, generally in the same night, to facilitate cosmic ray rejection. Badenes et al. (2009) used these individual exposures to look for large radial velocity shifts (120 km s⁻¹ or more) and found one such object. There are 25 of our binary candidates that were also examined as part of their SWARMS survey (C. Badenes 2010, private communication). In most cases, no obvious radial velocity shifts can be detected. For J002322.44+150011.6, however, a strong cross correlation is observed between individual exposures and there is a hint of a large velocity shift although the lines are very weak. 8-meter class telescopes will obviously be needed to achieve good radial

⁸We note that the shape of $H\alpha$ is a poor diagnostic, since the dilution by a DC produces an *apparent* broadening similar to the real enhanced broadening of a dense helium-rich atmosphere.

velocity measurements for our faint candidates.

3.5. Helium-Rich DA White Dwarfs

Bergeron et al. (1991) were the first to show on a quantitative basis that the pressure effects produced on the hydrogen lines in a cool ($T_{\text{eff}} \lesssim 12,000$ K) DA star with a high surface gravity could not be distinguished from those produced by the presence of large amounts of helium. The authors also suggested that the higher than average $\log g$ values inferred from spectroscopic analyses of cool DA stars could be the result of the presence of helium brought to the surface by convective mixing. But the non-detection of He I lines in high-resolution Keck observations of cool DA stars by Tremblay et al. (2010) ruled out the systematic presence of helium in these atmospheres. However, there are rare white dwarfs, such as GD 362 and HS 0146+1847, that were interpreted as massive DA stars, but the detection of the weak He I $\lambda 5877$ line in high-resolution spectroscopic data suggested instead that these stars had normal masses with helium dominated atmospheres (Koester et al. 2005; Zuckerman et al. 2007). Both of these white dwarfs are DAZ stars with circumstellar disks, and the source of hydrogen and metals in these helium-dominated atmospheres is likely due to accretion from a water-rich asteroid (Jura et al. 2009).

Broad and shallow H α features are also observed in cool white dwarfs, indicative of a trace of hydrogen ($\text{H}/\text{He} \sim 10^{-3}$) in a helium-dominated atmosphere (see, e.g., Fig. 12 of Bergeron et al. 2001). The hottest of these objects is the DZA white dwarf Ross 640 at $T_{\text{eff}} \sim 8500$ K. While no circumstellar disk has been reported for this object, the simultaneous presence of metals in its spectrum again suggests an external source for hydrogen. Alternatively, the presence of mixed H/He compositions could be the result of the mixing of the thin superficial hydrogen atmosphere with the deeper and more massive helium convection zone (Tremblay & Bergeron 2008). White dwarfs with mixed atmospheric compositions become increasingly common at even cooler temperatures ($T_{\text{eff}} \lesssim 6000$ K) where they can be easily identified from their strong infrared flux deficiency due to collision-induced absorption by molecular hydrogen (Kilic et al. 2010).

We identified in our SDSS sample two cool and massive DA white dwarfs, J090150.74+091211.3 and J170204.81+593635.5, that we believe are probably helium-rich objects. These stars were initially flagged as 2σ outliers in the T_{phot} vs. T_{spec} diagram shown in Figure 8, but we were unable to fit them with binary models. In both cases, the photometric temperature was significantly larger than the spectroscopic value (by 23% and 37%, respectively), and the $\log g$ value was unusually high (9.89 and 9.66, respectively). In Figure 15, we present our best fits assuming helium-rich compositions. Because of the degeneracy between surface gravity

and helium abundance, we simply assume here a value of $\log g = 8$. For the photometric fits, both the surface gravity and the hydrogen abundance are fixed, the latter set at the spectroscopic value. We can see that the spectroscopic and photometric temperatures are now in agreement to within $\sim 10\%$, which shows that by relying on *ugriz* observations, one can partially break the degeneracy between extremely high $\log g$ stars and normal mass helium-rich objects.

The first object in Figure 15, J170204.81+593635.5, is also a DAZ white dwarf with the obvious Ca II $\lambda 3969$ blended with H ϵ . It appears like a cooler counterpart of GD 362 and HS 0146+1847, although with significantly smaller metal abundances. It would be interesting to confirm if the simultaneous presence of hydrogen and metals in the photosphere of this star could be explained by the existence of a circumstellar disk. The second object shown in Figure 15, J090150.74+091211.3, is even cooler at $T_{\text{eff}} \sim 8500$ K, and is similar to Ross 640 in terms of temperature and hydrogen abundance, even though no metal lines are detected in the spectrum of this object. These helium-rich white dwarf candidates are also interesting because they bridge the temperature gap between DAZ white dwarfs like GD 362 and Ross 640. Obviously, higher S/N spectroscopic observations and trigonometric parallax measurements would help to confirm our interpretation of these stars, although these measurements for such faint ($g \sim 18.5$) objects are admittedly difficult to secure.

4. DISCUSSION

4.1. Reappraisal of Previous Analyses of the SDSS Data Release 4

Prior to this work, individual atmospheric parameters for most stars in the DR4 catalog could only be found in the original Eisenstein et al. (2006) paper. These authors were careful to define the largest white dwarf sample ever identified so far, but their spectroscopic analysis was preliminary, and as emphasized by the authors, their `autofit` program was only designed to offer a first-pass estimate of temperatures and surface gravities and to flag outliers. Also, most spectroscopic fits were not visually and individually inspected, unlike in our analysis. The model atmospheres between both analyses differ as well. In particular, our models rely on improved Stark broadening profiles and we also account for NLTE effects at high temperatures. Our atmospheric parameters should thus represent a significant improvement over previous estimates, especially given the latest improved DR7 data reduction (Kleinman et al. 2009).

In Figure 16, we compare our atmospheric parameters with those obtained by Eisenstein et al. (2006). The agreement is surprisingly good considering the differences in the data reduction,

model spectra, and fitting procedures. We find very few outliers, which implies that both fitting techniques are robust, the main exception being the DA–M dwarf binaries, although Eisenstein et al. stress that their atmospheric parameters are appropriate only if the spectral classification is DA or DB, without other subtle variations. We note that our surface gravities are significantly lower at cool temperatures ($T_{\text{eff}} \lesssim 8500$ K, by as much as 1 dex), most likely due to the fact that the models used by Eisenstein et al. only include Stark and Doppler broadening (see also Section 2 of Kepler et al. 2007 where similar models are used), while our models also take into account neutral broadening. Finally, most subtypes identified here are identical to those reported in Eisenstein et al. In addition to the double degenerate candidates reported in Table 3, there are 36 objects in Table 1 for which our classification differs from that of Eisenstein et al. Most of them have faint or questionable features (Zeeman splitting, M–Dwarf contamination and He II or Ca lines) and our different classifications might only result from different thresholds in the detection of these features. We thus conclude that the `autofit` program and method of analysis employed by Eisenstein et al. are reasonable, except that a more careful visual inspection would identify additional subtypes and problematic observations, which is an essential step in determining individual parameters for these stars, and to compute accurate mean values for the sample.

The second important study of the DA stars in the DR4 is that of Kepler et al. (2007) who went further and mainly focused on the mass distribution of the sample, neglecting subtypes (DA–M dwarf binaries, magnetics, DAZ, and DAB stars), as we did in Section 3.2. They used a more extensive model grid than that of Eisenstein et al. (2006), but the physics included in these models is similar. Even though Kepler et al. argue that the fits at low effective temperatures cannot be trusted since this corresponds to the temperature range where the high- $\log g$ problem is encountered, we believe that a proper understanding of this problem begins with the best achievable analysis of these cool DA stars. Furthermore, it is not explicitly stated in Kepler et al. (2007) whether individual fits were visually examined in order to define a clean sample of single white dwarfs.

The optimal way of comparing our mean mass determination to that of Kepler et al. (2007) would be to start with a 1:1 study of individual objects, to evaluate the differences in the models and sample selections, as noted above, and also in the fitting procedures⁹. Unfortunately, since individual atmospheric parameters were not published in their work, a

⁹Kepler et al.’s fitting method includes the full spectrophotometric spectra, which they argue provides the lowest internal uncertainties. One should be cautious, however, with external uncertainties stemming from data reduction, such as those presented in Figure 4 (bottom panel) and discussed in Section 3.1. While we do not claim that our fitting method is better, we suggest that it is equivalent, and more easily comparable to other DA surveys, which rely on an approach similar to ours.

detailed comparison is not possible here, and only average values can be compared. We note that Kepler et al. still give the atmospheric parameters of some low-mass and high-mass outliers identified in their mass distribution, a discussion we postpone to Section 4.5.

We recomputed the mean mass of our sample in the range $100,000 \text{ K} > T_{\text{eff}} > 12,000 \text{ K}$, i.e. the same range of temperature used by Kepler et al. (2007), and we find the same value as before, $\langle M \rangle = 0.61 M_{\odot}$, which can be compared to the value reported by Kepler et al., $\langle M \rangle = 0.59 M_{\odot}$. This small difference is entirely consistent with the shift produced by the use of our improved Stark profiles, and it is comparable to the shift observed for the PG sample (Tremblay & Bergeron 2009) where we found a significantly higher mean mass (by $\sim 5\%$) compared to calculations with older models. This suggests that the effects of using different model spectra, data reductions, sample selections, and fitting techniques, are small, after all.

4.2. Comparison with Bright DA White Dwarfs

We now compare our results for the DA stars in the SDSS with the ongoing spectroscopic survey of bright ($V \lesssim 17$) DA white dwarfs of Gianninas et al. (2011) drawn from the Villanova White Dwarf Catalog (McCook & Sion 1999). The obvious advantage of this comparison is that we are using the same model atmospheres and fitting technique in both analyses, and therefore any disparity can be attributed to differences in the sets of observations only. Unlike the SDSS spectra, however, the wavelength coverage used in the Gianninas et al. survey does not extend to $\text{H}\alpha$. We thus repeated our analysis of the SDSS spectra without including $\text{H}\alpha$ in our fitting procedure, and found nearly identical results. We can therefore safely compare the results between both surveys without further ado.

We find 89 stars in common between both surveys. These correspond of course to the brightest DA stars in the SDSS, which were already known prior to that survey. The comparison between both sets of atmospheric parameters is displayed in Figure 17. We can see that the SDSS temperatures are systematically larger by about 2%, on average, in the range $40,000 > T_{\text{eff}} > 13,000 \text{ K}$, than those obtained using the Gianninas et al. spectra, while the $\log g$ values are lower by about 0.06 dex, on average, in the same range of temperature, with differences increasing at higher effective temperatures. As mentioned above, since we are using the same theoretical framework and fitting method, these differences can only be attributed to the use of different spectra.

We compare in Table 4 the values of the mean mass, the standard deviation, as well as the median mass for the SDSS sample, the Gianninas et al. sample, and the PG sample

(Liebert et al. 2005); note that the PG sample is a subset of the Gianninas et al. sample. The mean mass is quite sensitive to the number of low-mass and high-mass outliers in each sample, while the median mass is more closely related to the peak value of the mass distribution. For internal consistency, we use the same range of effective temperatures to determine the average properties of each sample. We also remove all magnetic stars, double degenerates, and DA–M dwarf composite systems. We should mention that the PG sample has already been analyzed in Tremblay & Bergeron (2009) but the values reported here differ slightly from those published as a result of three minor improvements in our analysis: the addition of the nonideal electronic perturbations in the equation of state (see Section 2.2), our slightly different line normalization technique (see Section 2.3), and our exclusion of DA subtypes, which all contribute to lower the mean mass.

We first notice that the values of the mean mass and standard deviation for the Gianninas et al. sample are slightly larger than the PG sample, although their median masses are nearly identical. This suggests that there are a bit more high-mass outliers in the Gianninas et al. sample, which is not surprising since the Villanova White Dwarf Catalog contains a large number of massive white dwarfs detected in X-ray surveys (see, e.g., Vennes 1999). Therefore, we feel it is more appropriate, in what follows, to restrict our comparison to median values only.

The results presented in Table 4 indicate that the median mass of the SDSS sample is about $0.02 M_{\odot}$ lower than the PG and Gianninas et al. samples (corresponding to a $\log g$ value ~ 0.04 dex lower). This difference is of course consistent with the results shown in the bottom panel of Figure 17, which compares $\log g$ values for objects in common between SDSS and Gianninas et al. We must then conclude that the differences in the median values are mostly likely due to problems in the data reduction rather than to selection effects. Since the Gianninas et al. sample includes white dwarf spectra secured over many years using various telescopes and instruments, systematic data reduction effects are less likely to be present. Furthermore, problems with the calibration of the SDSS spectra have been known to exist in the first few data releases (Kleinman et al. 2004; Eisenstein et al. 2006). Even though these are believed to have been fixed in the new Data Release 7 (Kleinman et al. 2009), we suggest here that a small ($\sim 3\%$) but systematic calibration problem may still remain. As discussed in Section 3.3, a systematic shift in the spectroscopic temperatures could also explain part of the problem observed in the comparison with photometric temperatures.

Another way to look at this problem is to compare the mass distribution as a function of effective temperature for both the SDSS and Gianninas et al. samples, as shown in Figure 18. We first notice that the number of high-mass outliers is larger in the Gianninas et al. sample due to the selection effects discussed above; the most massive white dwarfs in

this distribution are actually ROSAT objects. We thus prefer to focus our attention on the peak of the distributions; lines of constant mass at $0.55 M_{\odot}$ and $0.70 M_{\odot}$ have been included in Figure 18 to guide the eye. It is obvious that there is a systematic offset between both distributions. The mass values in the SDSS increase from the hot end of the sequence down to about 12,500 K, while they remain more uniformly distributed around the mean in the Gianninas et al. sample. We note that the Gianninas et al. distribution was shown to be more uniform (Tremblay et al. 2010) when using the improved model spectra from Tremblay & Bergeron (2009). These results reinforce our conclusions that a problem with the calibration of the SDSS spectra still exists, even in the latest data release.

We finish this section with a short discussion of the cool end ($T_{\text{eff}} \lesssim 13,000$ K) of the mass distribution shown in the top panel of Figure 18, where close to half of the SDSS stars are located. We can clearly see an important increase in the mean mass in this particular range of temperature, which corresponds to the well known high- $\log g$ problem discussed at length by Koester et al. (2009) and Tremblay et al. (2010). These unrealistic mass values prevent us from going much further in the analysis of these cool DA stars, but the mass distribution can prove itself useful in better understanding the nature of this problem. To better illustrate the shift in the mean mass, we average in Figure 19 the distribution into temperature bins of 1000 K, and compute the corresponding mass standard deviation. We observe that the SDSS mass distribution exhibits an important and distinct triangular bump, with the mass dispersion remaining fairly small and constant as a function of temperature, even down to the very cool end of the distribution. The fact that the mean mass appears to *decrease* again below 10,000 K should be viewed with caution, however, since our model atmosphere calculations include a free parameter in the treatment of the nonideal effects from neutral particles, which allows some extra leverage to “calibrate” the $\log g$ values (see Section 5.1 of Tremblay et al. 2010). The SDSS sample definitely provides the clearest picture so far of the high- $\log g$ problem, and it will certainly be helpful in future investigations of this problem.

4.3. Hot DA and DAO White Dwarfs

We have postponed our discussion of the 184 hot DA stars ($T_{\text{eff}} > 40,000$ K) until now due to the few extra steps needed to analyze these objects. First of all, we uncovered 17 hot DAO stars in the SDSS-E06 catalog, characterized by the He II $\lambda 4686$ absorption line. All but two of these objects were previously classified as DAO in the SDSS-E06 (the DAO J130815.21–015904.4 and DAO+dM J094720.94+111734.7 were identified as DA and DA+dM, respectively). We observe the so-called Balmer-line problem (see Gianninas et al.

2010, and references therein) in all of these DAO stars, but also in many of our hot DA stars, especially at $H\alpha$ and $H\beta$. This problem manifests itself as an inability of the model spectra to reproduce simultaneously all Balmer line profiles. A solution to the Balmer-line problem was presented by Werner (1996) when they included carbon, nitrogen, and oxygen (CNO) – with proper Stark broadening – in their model atmospheres. The main effect is a cooling of the upper layers of the atmospheres, the formation region of the core of the lower Balmer lines. These improved models are shown to provide much better fits to the observed line profiles. More reliable atmospheric parameters are then obtained, even if the CNO metals are merely a proxy for all metals in the atmosphere and it is by no means a determination of the CNO abundances. The 15 DAO stars identified in the SDSS-E06 have already been analyzed with mixed H/He models by Hügelmeyer et al. (2007)¹⁰ but without metals included in the model calculations to account for the Balmer-line problem.

We rely upon the NLTE model atmospheres with homogeneous H/He/CNO compositions introduced by Gianninas et al. (2010) to fit the DAO stars in our SDSS sample. These models, computed with TLUSTY and using improved Stark broadening from Tremblay & Bergeron (2009), are similar to the pure hydrogen models presented in Section 2.2 except for their chemical compositions. The CNO metal abundances are fixed at the Asplund et al. (2005) solar values. Our fitting procedure is very similar to the one previously described in this work, except that we also fit the helium abundance based on the profile of He II $\lambda 4686$. The improved atmospheric parameters for 16 DAO stars are presented in Table 5. The DAO–dM composite system J094720.94+111734.7 is instead fitted with regular DA models since the $H\alpha$ and $H\beta$ lines are contaminated by the M dwarf, and the parameters are given in Table 1. We also find that 27 hot DA stars in SDSS show the Balmer-line problem (DA+BP). We fitted these objects with the H/CNO models also discussed in Gianninas et al. (2010); the atmospheric parameters are reported in Table 1 (see Note 6). The Balmer-line problem is resolved for the majority of the 43 DAO and DA+BP objects fitted with CNO models. Also, the fits without CNO tend to underestimate surface gravities by ~ 0.1 - 0.2 dex (see also Gianninas et al. 2010 for more details), hence the effects are important on the properties of the hot end of the SDSS mass distribution.

The size of our sample of hot DA white dwarfs is similar to that of Gianninas et al. (2010), who analyzed 152 DA stars above $T_{\text{eff}} > 40,000$ K. The fraction of objects showing the Balmer line problem is roughly the same, suggesting that this discrepancy can be efficiently detected even at the lower average S/N of the SDSS sample. The additional diagnostic that can be performed with $H\alpha$ in the SDSS helps in identifying the Balmer-line

¹⁰Their sample also includes J163200.32–001928.3, clearly a DAO star but identified as a DO in the SDSS-E06 catalog, hence it was not selected in this work.

problem at lower S/N. In the course of our visual inspection, however, it was obvious that only extreme DA+BP could be detected for some objects with $S/N < 20$. The atmospheric parameters of hot DA stars below this threshold should therefore be viewed as a pure hydrogen approximation.

In Figure 18, both the SDSS and Gianninas et al. mass distributions include the improved atmospheric parameters of objects fitted with H/He/CNO models. We find a mean mass of $\langle M \rangle = 0.54 M_{\odot}$ for our SDSS hot DA sample, which is significantly lower than mean mass identified for cooler stars. This is expected, however, considering that the data reduction problem identified in the previous section is worse at the hot end of the distribution (see Figures 17 and 18). For the DAO stars, we obtain a mean mass of $\langle M \rangle = 0.52 M_{\odot}$, a value very similar to the hot DAs, which further confirms the suggestion of Gianninas et al. (2010) that the DA and DAO share a common history. If we make abstraction of the reduction problem, it is very interesting to note that in both the SDSS and Gianninas et al. surveys, the hot end of the mass distribution is a smooth continuation of the sequence at cooler temperatures. This result is a direct consequence of the new models computed in Gianninas et al. (2010), including NLTE effects, CNO metals (for a majority of stars at $\log T_{\text{eff}} > 4.8$) and improved Stark broadened profiles.

4.4. White Dwarf–M Dwarf Binaries

We analyzed in our study a large number of DA–M dwarf binaries that are part of the DR4 sample. Their atmospheric parameters are given in Table 1, although these were not included in the calculations of the mean properties of the SDSS sample in order to define a cleaner sample of single DA stars. Most of these objects have already been analyzed in detail by Silvestri et al. (2006) and Heller et al. (2009), although both studies were not necessarily restricted to the DR4 sample. One of the reason is that the SDSS-E06 catalog was not meant to be complete in terms of the white dwarf–M dwarf binary content. The colors of these objects can be significantly different from those of single white dwarfs, especially when the total flux is dominated by the M dwarf (i.e., the colors are very red). In those cases, the object colors can be close to the low-mass end of the main-sequence stellar locus, and rejected by the cutoffs. In contrast, Silvestri et al. (2006) resorted to an algorithm to automatically identify spectral features of white dwarfs in all DR4 spectra in addition to the color selection. They claim that their sample comprises almost all spectroscopically observed DA–M dwarf in the SDSS up to Data Release 4.

The deconvolution technique developed by Heller et al. (2009) is the most sophisticated in terms of the determination of the atmospheric parameters of both the DA white dwarf

and the main sequence companion. They fit simultaneously the effective temperature and surface gravity of both stars, as well as the metallicity of the M dwarf component. However, the precision on the white dwarf parameters is rather low, with uncertainties as large as 0.5 dex in $\log g$. This approach is not really convenient in the present context since we are mostly interested in the white dwarf component of the system. Silvestri et al. (2006) developed a more approximate method to fit the main sequence star by using a series of spectral templates with average atmospheric parameters. Then, by iteration, they subtracted the contribution of the M dwarf component until a clean white dwarf spectrum is obtained. This procedure has some flaws since it is not possible to completely remove all spectral features from the M dwarf companion, but it still allows a larger number of Balmer lines to be fitted in comparison with the contaminated spectrum.

We compare in Figure 20 our atmospheric parameters — determined by simply excluding from the χ^2 fit the Balmer lines that are contaminated by the M dwarf companion — with those of Silvestri et al. (2006). We find a very good agreement between both sets of measurements, especially considering the differences in the model atmospheres. Our values of T_{eff} and $\log g$ are slightly larger, on average, than those of Silvestri et al., but this small offset is entirely consistent with our use of the improved Stark profiles of Tremblay & Bergeron (2009). These comparisons are similar to those shown in Figure 16 for single stars, which suggests that our method for fitting DA–M dwarf binaries is fairly reasonable and comparable to that of Silvestri et al. There are also a few outliers observed in Figure 20, which are explained by the particular choice between the cool or hot solutions for the DA star. It is a more complicated choice when analyzing such systems, with any fitting method, but we believe our identifications are good since our model fluxes are well matched by the observed $u - g$ color index.

We finally show in Figure 21 the mass distribution of the DA–M dwarf binaries in our SDSS sample, which can be compared to that for single stars displayed in Figure 7. The average masses and the shape of both distributions are clearly different. It is perhaps not surprising that the high-mass tail is absent from the DA–M dwarf mass distribution since massive white dwarfs have smaller radii and are less luminous, and they can thus be easily overshadowed by their M dwarf companion. But even the peak of the mass distribution appears at a slightly lower value than for single stars, a conclusion that can also be reached by looking at Figure 6 of Silvestri et al. (2006). Given these selection effects, it is difficult to conclude whether the observed differences are real, another reason why we have refrained from including these white dwarfs in our computation of the average properties of DA stars.

4.5. Outstanding Objects

Several extreme low-mass and high-mass white dwarfs have been identified in the SDSS and these have been the subject of numerous studies, including that of Kepler et al. (2007, see their Section 7). We find that our improved line profiles do not affect significantly the results of these earlier analyses. The shift in $\log g$ of these extreme mass white dwarfs is comparable to that of typical DA stars. For example, we find a value of $\log g = 6.40$ for J123410.36–022802.8, a value similar to that obtained by Liebert et al. (2004), $\log g = 6.38$, based on the same SDSS spectrum and a similar fitting method. This object was later reobserved by Kilic et al. (2007) at higher signal-to-noise ratio using the MMT, and we simply refer to their analysis for a determination of improved parameters for this star, as well as for other low-mass white dwarf candidates identified in the SDSS (see their Table 1).

For extreme high-mass white dwarfs close to the Chandrasekhar limit, the asymptotic relation between surface gravity and mass implies that a typical change in the value of $\log g$ will result only in a negligible change in mass. Therefore, we do not expect significant changes compared to published values. And as it turns out, our mass determinations for the most massive white dwarfs in our sample are in the same range as those reported in Table 6 of Kepler et al. (2007). We should note, however, that some of them have been flagged in our Table 1 as problematic observations (e.g., J155238.21+003910.3 and J110735.32+085924.5) and one should thus be cautious about their mass determinations. Furthermore, we suspect that some of the lower S/N candidates could be weakly magnetic stars. For instance, J154305.67+343223.6, identified in Table 6 of Kepler et al., is actually a magnetic white dwarf (Külebi et al. 2009). We believe that in any case, higher S/N observations are required to properly constrain the mass of these stars (these objects are indeed extremely faint with $18 < g < 19$).

5. CONCLUSION

We presented an updated spectroscopic analysis of the DA white dwarfs identified in the SDSS Data Release 4 catalog of Eisenstein et al. (2006), with the most recent data reduction from DR7, using our improved NLTE model grid including Stark profiles with non-ideal gas effects (Tremblay & Bergeron 2009; Tremblay et al. 2010). A careful visual inspection of each individual spectroscopic fit ($S/N > 12$), together with a comparison with *ugriz* photometric fits, allowed us to obtain a significantly cleaner sample and improved atmospheric parameters for these DA stars compared to previous studies.

We also performed a simulation of DA+DA and DA+DB/DC double degenerate bi-

naries analyzed both photometrically and spectroscopically using single DA star models. We showed that DA+DA unresolved binaries could not be easily detected with the SDSS data, but that most DA+DB/DC systems would appear as outliers when comparing spectroscopic and photometric temperatures. Using this approach, we were able to identify 35 DA+DB/DC double degenerate candidates in the SDSS sample, most of them discussed for the first time in our analysis. We find, however, that it is rather difficult to confirm unambiguously our interpretation of the binary nature of DA+DC candidates at low S/N since these objects can easily be mistaken for magnetic white dwarfs or helium-rich DA stars.

We evaluated that a lower cutoff at $S/N = 15$ in the computation of the mean mass of DA white dwarfs provides the best statistical significance for these stars in the SDSS sample. Our calculations yielded a mean mass of $0.613 M_{\odot}$ compared to a value $0.593 M_{\odot}$ previously reported by Kepler et al. (2007). This difference is entirely consistent with the shift of $\sim 0.03 M_{\odot}$ expected from our improved models. We also compared our results for bright DA stars in common between the SDSS survey and the Villanova White Dwarf Catalog sample of Gianninas et al. (2011) using the same grid of model atmospheres and fitting techniques. We unexpectedly found a mean mass for this subsample that is significantly higher (by $\sim 0.03 M_{\odot}$) in the Gianninas et al. survey. We concluded that a small problem with the data reduction still remains in the spectroscopic calibration of the SDSS Data Release 7.

Since no white dwarf survey is as large in volume as the SDSS, resolving this issue will be important to characterize the mass distribution of DA stars using SDSS data. This will also help in understanding the absolute temperature scale of DA white dwarfs, for which an offset is actually observed between spectroscopic and photometric temperatures. Inevitably, this work will also be beneficial as a guide for the analysis of new objects identified in the SDSS Data Release 7, which are likely to have properties very similar to those identified here.

We thank Carles Badenes, Vincent Cardin, and Audrey Maiuro for their contribution to this project. This work was supported by the NSERC Canada and by the Fund FQRNT (Québec).

REFERENCES

- Abazajian, K. N., et al. 2009, *ApJS*, 182, 543
- Althaus, L. G., Serenelli, A. M., & Benvenuto, O. G. 2001, *MNRAS*, 323, 471
- Asplund, M., Grevesse, N., & Sauval, A. J. 2005, in *ASP Conf. Ser. 336, Cosmic Abundances as Records of Stellar Evolution and Nucleosynthesis*, eds. T. G. Barnes III & F. N. Bash, (San Francisco: ASP), 25
- Badenes, C., Mullally, F., Thompson, S. E., & Lupton, R. H. 2009, *ApJ*, 707, 971
- Beauchamp, A., Wesemael, F., Bergeron, P., Liebert, J., & Saffer, R. A. 1996, in *ASP Conf. Ser. Vol. 96, Hydrogen-Deficient Stars*, ed. S. Jeffery & U. Heber (San Francisco: ASP), 295
- Bergeron, P., Leggett, S. K., & Ruiz, M. T. 2001, *ApJS*, 133, 413
- Bergeron, P., Saffer, R. A., & Liebert, J. 1992, *ApJ*, 394, 228
- Bergeron, P., Wesemael, F., & Fontaine, G. 1991, *ApJ*, 367, 253
- Bergeron, P., Wesemael, F., Lamontagne, R., Fontaine, G., Saffer, R. A., & Allard, N. F. 1995, *ApJ*, 449, 258
- DeGennaro, S., von Hippel, T., Winget, D. E., Kepler, S. O., Nitta, A., Koester, D., & Althaus, L. 2008, *AJ*, 135, 1
- Dufour, P., Liebert, J., Fontaine, G., & Behara, N. 2007, *Nature*, 450, 522
- Eisenstein, D. J., et al. 2006, *ApJS*, 167, 40
- Fontaine, G., Brassard, P., & Bergeron, P. 2001, *PASP*, 113, 409
- Gianninas, A., Bergeron, P., Dupuis, J., & Ruiz, M. T. 2010, *ApJ*, 720, 581
- Gianninas, A., Bergeron, P. & Fontaine, G. 2005, *ApJ*, 631, 1100
- Gianninas, A., Bergeron, P., & Ruiz, M. T. 2009, *Journal of Physics Conference Series*, 172, 012021
- Gianninas, A., Bergeron, P., & Ruiz, M. T. 2011, *ApJ*, in preparation
- Hamada, T., & Salpeter, E. E. 1961, *ApJ*, 134, 683

- Harris, H. C., et al. 2003, *AJ*, 126, 1023
- Harris, H. C., et al. 2006, *ApJ*, 131, 571
- Heller, R., Homeier, D., Dreizler, S., & Østensen, R. 2009, *A&A*, 496, 191
- Holberg, J. B., & Bergeron, P. 2006, *ApJ*, 132, 1221
- Hubeny, I., & Lanz, T. 1995, *ApJ*, 439, 875
- Hügelmeier, S. D., Dreizler, S., Rauch, T., & Krzesiński, J. 2007 in *Proc. 15th European Workshop on White Dwarfs*, eds. R. Napiwotzki & M. Burleigh (San Francisco: ASP), 372, 187
- Hummer, D. G., & Mihalas, D. 1988, *ApJ*, 331, 794
- Jura, M., Munro, M. P., Farihi, J., & Zuckerman, B. 2009, *ApJ*, 699, 1473
- Kepler, S. O., Kleinman, S. J., Nitta, A., Koester, D., Castanheira, B. G., Giovannini, O., Costa, A. F. M., & Althaus, L. 2007, *MNRAS*, 375, 1315
- Kilic, M., Allende Prieto, C., Brown, W. R., & Koester, D. 2007, *ApJ*, 660, 1451
- Kilic, M., et al. 2010, *ApJS*, 190, 77
- Kleinman, S. J., et al. 2004, *ApJ*, 607, 426
- Kleinman, S. J., Nitta, A., & Koester, D. 2009, *Journal of Physics Conference Series*, 172, 012020
- Koester, D., Kepler, S. O., Kleinman, S. J., & Nitta, A. 2009, *Journal of Physics Conference Series*, 172, 012006
- Koester, D., Napiwotzki, R., Voss, B., Homeier, D., & Reimers, D. 2005, *A&A*, 439, 317
- Külebi, B., Jordan, S., Euchner, F., Gänsicke, B. T., & Hirsch, H. 2009, *A&A*, 506, 1341
- Lemke, M. 1997, *A&AS*, 122, 285
- Liebert, J., Bergeron, P., Eisenstein, D., Harris, H. C., Kleinman, S. J., Nitta, A., & Krzesiński, J. 2004, *ApJ*, 606, L147
- Liebert, J., Bergeron, P., & Holberg, J. B. 2005, *ApJS*, 156, 47

- Liebert, J., Bergeron, P., & Saffer, R.A. 1991, in 7th European Workshop on White Dwarfs, NATO ASI Series, ed. G. Vauclair & E. M. Sion (Dordrecht: Kluwer Academic Publishers), 409
- Limoges, M.-M., & Bergeron, P. 2010, *ApJ*, 714, 1037
- McCook, G. P., & Sion, E. M. 1999, *ApJS*, 121, 1
- Schmidt, G. D., et al. 2003, *ApJ*, 595, 1101
- Silvestri, N. M., et al. 2006, *AJ*, 131, 1674
- Tremblay, P.-E., & Bergeron, P. 2008, *ApJ*, 672, 1144
- Tremblay, P.-E., & Bergeron, P. 2009, *ApJ*, 696, 1755
- Tremblay, P.-E., Bergeron, P., Kalirai, J. S., & Gianninas, A. 2010, *ApJ*, 712, 1345
- Vanlandingham, K. M., et al. 2005, *AJ*, 130, 734
- Vennes, S. 1999, *ApJ*, 525, 995
- Werner, K. 1996, *ApJ*, 457, L39
- Wesemael, F., et al. 1994, *ApJ*, 429, 369
- Wood, M. A. 1995, in 9th European Workshop on White Dwarfs, NATO ASI Series, ed. D. Koester & K. Werner (Berlin: Springer), 41
- York, D. G., et al. 2000, *AJ*, 120, 1579
- Zuckerman, B., Koester, D., Melis, C., Hansen, B. M., & Jura, M. 2007, *ApJ*, 671, 872

Table 1. SDSS DR4 Sample of DA White Dwarfs with S/N > 12

SDSS name	Plate–MJD–Fiber	T_{eff} (K)	$\log g$	M/M_{\odot}	M_V	$\log \tau$	Notes
J000006.75–004653.8	0685-52203-225	10850 (160)	8.39 (0.10)	0.85 (0.07)	12.52	8.95	
J000022.53–105142.1	0650-52143-217	8620 (110)	8.31 (0.15)	0.79 (0.10)	13.24	9.18	1
J000022.87–000635.7	0387-51791-166	23010 (470)	7.44 (0.06)	0.42 (0.01)	9.57	7.59	
J000034.07–010819.9	0685-52203-187	13090 (220)	8.01 (0.05)	0.61 (0.03)	11.52	8.50	
J000104.05+000355.8	0685-52203-490	13710 (600)	8.06 (0.08)	0.64 (0.05)	11.51	8.50	
J000127.48+003759.1	0685-52203-491	18560 (490)	7.84 (0.09)	0.53 (0.04)	10.66	7.88	
J000308.32–094147.0	0650-52143-550	8690 (90)	8.50 (0.12)	0.92 (0.08)	13.53	9.36	
J000357.63–004939.1	0387-51791-005	9740 (100)	8.95 (0.10)	1.18 (0.04)	13.98	9.41	
J000428.98+005801.9	0685-52203-621	16410 (500)	7.85 (0.10)	0.54 (0.05)	10.90	8.10	
J000441.75+152841.1	0751-52251-393	8710 (60)	8.20 (0.09)	0.72 (0.06)	13.02	9.07	
J000622.61+010958.7	0388-51793-448	39040 (1930)	7.73 (0.23)	0.54 (0.09)	9.03	6.69	
J000630.56+002323.9	0388-51793-424	23590 (770)	7.89 (0.11)	0.58 (0.06)	10.30	7.45	
J000636.61+160237.7	0751-52251-528	9620 (100)	8.30 (0.12)	0.79 (0.08)	12.80	9.03	
J000716.84–101908.4	0651-52141-230	20150 (740)	7.87 (0.11)	0.55 (0.06)	10.56	7.75	
J000737.18–090629.3	0651-52141-416	20240 (410)	7.88 (0.06)	0.56 (0.03)	10.56	7.71	
J000738.03+004003.3	1490-52994-507	10460 (70)	8.32 (0.06)	0.81 (0.04)	12.53	8.95	
J000946.45+144310.6	0751-52251-101	24570 (240)	7.89 (0.03)	0.57 (0.02)	10.22	7.31	
J001038.78–003241.5	0388-51793-074	10240 (120)	8.47 (0.11)	0.90 (0.07)	12.86	9.10	
J001148.19–092110.2	0652-52138-348	12680 (180)	7.84 (0.06)	0.52 (0.03)	11.34	8.43	
J001245.60+143956.4	0752-52251-221	11270 (120)	7.89 (0.07)	0.54 (0.04)	11.65	8.60	
J001339.19+001924.3	0389-51795-431	9600 (10)	8.32 (0.02)	0.80 (0.01)	12.84	9.04	2
J001415.59–103505.8	0651-52141-023	9920 (90)	8.42 (0.09)	0.86 (0.06)	12.87	9.09	
J001427.04+135058.4	0752-52251-135	8870 (60)	8.32 (0.08)	0.80 (0.05)	13.15	9.14	
J001448.82+002027.3	0687-52518-468	8960 (90)	8.08 (0.13)	0.64 (0.08)	12.72	8.97	2
J001518.88+135332.8	0752-52251-099	8590 (30)	8.20 (0.04)	0.72 (0.03)	13.08	9.09	
J001556.07–000515.3	0389-51795-493	9300 (80)	8.27 (0.10)	0.77 (0.06)	12.87	9.04	
J001629.05–004451.0	0687-52518-131	9640 (70)	8.30 (0.09)	0.79 (0.06)	12.78	9.02	
J001643.36+152410.8	0752-52251-584	8060 (60)	8.29 (0.09)	0.78 (0.06)	13.46	9.25	
J001654.67+151432.1	0752-52251-590	12870 (420)	8.23 (0.09)	0.75 (0.06)	11.87	8.68	
J001655.51–005604.5	0687-52518-100	16020 (270)	7.94 (0.05)	0.58 (0.03)	11.07	8.18	
J001747.15+155204.4	0752-52251-606	11800 (300)	8.35 (0.10)	0.83 (0.07)	12.23	8.85	
J001749.24–000955.5	0687-52518-109	54900 (1640)	7.47 (0.11)	0.50 (0.03)	8.11	6.11	3
J001836.15+003151.4	0688-52203-348	11850 (120)	8.12 (0.04)	0.68 (0.03)	11.85	8.67	2

Note. — Table 1 is available in its entirety in the electronic edition of the *Astrophysical Journal*. A portion is shown here for guidance regarding its form and content. (1) Incomplete wavelength coverage or glitches in the Balmer lines; (2) poor match between the slope of the observed spectra and the *ugriz* photometry; (3) main-sequence companion, one or two lines removed from the fit, and the line cores also removed due to emission; (4) same as previous but with no emission; (5) flagged in our visual inspection with a poor fit but no clear explanation was found; the atmospheric parameters under the assumption of a normal single DA should be regarded with caution; (6) DA with the Balmer-line problem and models with CNO were used; (7) emission in the line cores but no red excess; (8) DAZ; (9) DAO+dM. For one object where the fitted T_{eff} exceeds our models grid limit, we fix the parameters at $T_{\text{eff}} = 140,000$ K and $\log g = 8$.

Table 2. DA White Dwarfs with Multiple Measurements

S/N range	N ^a	$\langle\sigma_{\text{Teff}}\rangle^b$ (%)	$\langle\sigma_{\text{Teff-multiple}}\rangle^c$ (%)	$\langle\sigma_{\log g}\rangle^b$	$\langle\sigma_{\log g\text{-multiple}}\rangle^c$
$T_{\text{eff}} < 13,000$ K					
$12 < \langle\text{S/N}\rangle < 15$	18	1.3	1.0	0.12	0.14
$15 < \langle\text{S/N}\rangle < 20$	31	1.2	1.0	0.10	0.14
$\langle\text{S/N}\rangle > 20$	57	0.7	0.7	0.05	0.07
$T_{\text{eff}} > 13,000$ K					
$12 < \langle\text{S/N}\rangle < 15$	10	3.2	1.3	0.11	0.06
$15 < \langle\text{S/N}\rangle < 20$	24	2.7	2.6	0.08	0.07
$\langle\text{S/N}\rangle > 20$	54	1.8	1.8	0.05	0.05

^aNumber of stars with multiple measurements. Subtypes (DAO, DAZ, DA+dM and DA+DB) are not considered.

^bMean internal uncertainty from the fitting procedure.

^cAverage of the standard deviation between multiple observations.

Table 3. DA+DB/DC Binary Candidates

SDSS name	Plate-MJD-Fiber	T_{eff} (K) H-comp	$\log g$ H-comp	T_{eff} (K) He-comp	$\log g$ He-comp	Notes
J002322.44+150011.6	0753-52233-177	6490 (420)	8	10750 (390)	8	1,2
J015221.12-003037.3	0402-51793-114	34170 (1640)	7.87 (0.14)	14400 (3580)	8.05 (0.95)	3
J034229.97+002417.6	0714-52201-551	13420 (170)	8.32 (0.04)	14380 (160)	8.40 (0.06)	4
J040852.23-045504.7	0465-51910-482	7610 (200)	8	10730 (380)	8	2,5
J074436.39+451534.4	1737-53055-281	9640 (230)	8	6770 (580)	8	6
J080743.57+442148.0	0439-51877-188	8140 (170)	8.39 (0.14)	5380 (420)	8	5,6
J082403.91+310448.0	0931-52619-558	6080 (220)	8	10340 (210)	8	1,2
J083353.71+385218.8	0828-52317-277	26100 (1250)	8.01 (0.10)	16640 (910)	7.86 (0.17)	5
J084226.97+374040.0	0864-52320-524	12330 (300)	7.98 (0.20)	9030 (900)	8	
J084608.19+053818.0	1187-52708-630	9500 (260)	8.21 (0.16)	10040 (820)	8	6
J084742.22+000647.6	0467-51901-052	11840 (320)	8.19 (0.11)	17940 (790)	8.79 (0.15)	7
J084958.32+093847.7	1760-53086-411	10110 (320)	8.35 (0.13)	10410 (570)	8	5,6,7
J085159.31+532540.3	0449-51900-311	7120 (270)	8	10830 (370)	8	1,2
J085858.49+301231.3	1590-52974-148	12570 (290)	8.16 (0.09)	13830 (320)	8.33 (0.13)	
J093432.66+065848.6	1196-52733-093	38700 (1620)	7.52 (0.08)	27870 (9140)	7.71 (0.28)	5,7
J093944.64+371617.8	1275-52996-630	12800 (890)	8.05 (0.13)	13670 (530)	8	
J095902.54+451110.4	0942-52703-455	7060 (730)	8	8770 (2730)	8	2
J102003.38+000902.6	0271-51883-557	7120 (240)	8	10080 (710)	8	1,2
J102626.01+135745.0	1747-53075-430	7800 (230)	8	10650 (510)	8	1,2
J122143.98+590747.8	0955-52409-041	10390 (260)	7.99 (0.36)	9210 (1730)	8	6
J131907.32-023406.4	0341-51690-266	9520 (300)	8.29 (0.23)	14330 (630)	8.61 (0.30)	
J134259.26+530519.2	1042-52725-076	6420 (340)	8	11280 (220)	8	1,2
J140600.55+643312.9	0498-51984-163	11280 (310)	8.07 (0.17)	12650 (470)	8.11 (0.28)	
J141005.74-023500.2	0916-52378-266	7610 (470)	8	9870 (1760)	8	1,2
J141516.10-010912.1	0303-51615-057	8190 (170)	8	10650 (440)	8	6
J152145.91+393128.0	1293-52765-385	7070 (560)	8	9750 (2380)	8	1,2
J154710.83+442848.1	1333-52782-119	10700 (160)	8.24 (0.12)	6520 (510)	8	6
J162757.07+331346.1	1058-52520-221	10020 (150)	8.13 (0.16)	6710 (650)	8	6
J164306.05+442638.0	0629-52051-493	7740 (180)	8	10640 (390)	8	
J172037.26+271914.8	0979-52427-501	11840 (500)	8.23 (0.17)	14360 (530)	8.31 (0.25)	
J204036.43-001004.1	0981-52435-139	7760 (180)	8	11350 (280)	8	2
J210155.81-005745.0	0984-52442-049	12040 (180)	7.59 (0.07)	12340 (360)	7.96 (0.15)	5
J213819.85+112311.3	0731-52460-632	8810 (190)	8.57 (0.17)	7680 (770)	8	5
J223437.86+002111.7	0673-52162-630	12390 (560)	8.25 (0.19)	8370 (1000)	8	5,6
J224430.36+133430.2	0740-52263-264	11210 (300)	8	15160 (400)	8	

Note. — (1) Helium-rich DA an equally valid possibility; (2) very faint H lines, difficult to fit in any cases; (3) could also be a DAB; (4) also in Limoges & Bergeron (2010); (5) average photometric match; (6) weakly magnetic also a possibility, good photometric fit to a single star; (7) cores of the $H\alpha$ and $H\beta$ lines poorly fitted.

Table 4. Mean Properties of DA White Dwarf Samples

Sample	$\langle M/M_{\odot} \rangle$	Dispersion	Median Mass	Sample Description
SDSS	0.613	0.126	0.594	Eisenstein et al. (2006)
Palomar-Green	0.629	0.128	0.610	Liebert et al. (2005)
White Dwarf Catalog	0.638	0.143	0.610	Gianninas et al. (2009)

Table 5. SDSS DR4 Sample of DAO White Dwarfs with S/N > 12

SDSS name	Plate–MJD–Fiber	T_{eff} (K)	$\log g$	$\log \text{He/H}$	M/M_{\odot}	M_V	$\log \tau$
J034831.33+004616.3	1242-52901-412	90730 (2980)	7.15 (0.11)	−2.12 (0.18)	0.54 (0.02)	6.76	4.78
J081618.79+034234.1	1184-52641-171	51740 (3550)	7.53 (0.30)	−1.06 (0.39)	0.51 (0.10)	8.30	6.31
J082705.53+313008.2	0932-52620-126	78550 (2280)	7.33 (0.08)	−2.41 (0.13)	0.54 (0.02)	7.35	5.38
J101015.59+115711.3	1745-53061-218	52500 (2820)	7.38 (0.27)	−0.68 (0.22)	0.47 (0.08)	8.00	6.02
J120927.93−030206.2	0332-52367-184	79530 (4870)	7.13 (0.16)	−1.95 (0.25)	0.50 (0.04)	6.91	4.93
J121743.11+623118.2	0779-52342-152	98170 (5220)	6.98 (0.20)	−1.19 (0.19)	0.53 (0.04)	6.26	4.35
J125029.51+505317.3	1279-52736-450	71660 (13240)	7.08 (0.40)	−1.03 (0.61)	0.46 (0.11)	6.98	5.04
J130815.21−015904.4	0340-51691-358	53040 (1480)	7.73 (0.10)	−2.49 (0.25)	0.58 (0.04)	8.64	6.31
J131925.92+531715.0	1040-52722-015	96320 (16210)	6.73 (0.53)	−1.19 (0.52)	0.48 (0.11)	5.73	3.33
J135356.88−025630.4	0914-52721-214	53290 (1890)	7.76 (0.13)	−2.15 (0.28)	0.59 (0.05)	8.68	6.30
J145606.73+491116.5	1048-52736-619	93050 (6230)	6.64 (0.18)	−1.15 (0.19)	0.45 (0.05)	5.61	3.78
J153102.39+534900.6 ^a	0616-52442-320	78680 (7970)	6.85 (0.25)	−1.96 (0.40)	0.44 (0.06)	6.35	4.16
J160236.07+381950.5	1055-52761-473	84630 (5290)	7.03 (0.17)	−2.14 (0.28)	0.49 (0.04)	6.62	4.57
J161441.98+370548.1	1056-52764-546	55640 (1710)	7.66 (0.10)	−3.22 (0.34)	0.56 (0.04)	8.45	6.24
J170508.81+212019.2	1425-52913-570	50300 (1000)	7.67 (0.08)	−2.70 (0.24)	0.55 (0.03)	8.59	6.36
J235137.23+010844.2	0684-52523-370	89500 (8920)	7.56 (0.33)	−1.39 (0.40)	0.63 (0.09)	7.65	5.59

^aObservational glitch.

Fig. 1.— Left panel: distribution of S/N for all 8717 DA spectra in the SDSS-E06 sample. Right panel: S/N as a function of the observed g magnitude.

Fig. 2.— Sample fits for 20 DA stars in the SDSS sample with high signal-to-noise spectroscopic data ($S/N > 30$). The atmospheric parameters are given in each panel.

Fig. 3.— Mass distribution as a function of effective temperature for DA stars in the SDSS with $T_{\text{eff}} < 40,000$ K, for two separate ranges of S/N. Lines of constant mass at $0.55 M_{\odot}$ and $0.70 M_{\odot}$ are shown as a reference.

Fig. 4.— Sample fits of DA stars in the SDSS sample with the atmospheric parameters given in each panel (left panels). In the right panels, we show complementary data used in our visual inspection. The y-axis scale is fixed by the observed photometric fluxes (blue error bars) that are fitted with average model fluxes (blue filled dots). The photometric temperature is given in each panel. Both the fluxed spectra (in gray) and synthetic model fluxes (in red), calculated at the spectroscopic parameters given in the left panel, are then scaled to the r photometric band. The objects are discussed in the text.

Fig. 5.— Similar to Figure 4 for both the hot and cool spectroscopic solutions of J084226.97+374040.0 (top and bottom panels, respectively). The observed and model spectra on the left panels are binned by a factor of two for clarity. This object is actually a DA+DC binary candidate.

Fig. 6.— Top panel: mean mass of the DA stars in the SDSS as a function of the S/N of the observations. The objects have been separated in bins of nearly equal number of stars, identified by dotted vertical lines. Filled circles correspond to DA stars with $40,000 \text{ K} > T_{\text{eff}} > 13,000 \text{ K}$, while open circles represent cooler objects. Bottom panel: similar to the top panel but for the mass standard deviation as a function S/N.

Fig. 7.— Mass distribution for the DA stars in the SDSS with $40,000 \text{ K} > T_{\text{eff}} > 13,000 \text{ K}$. The distribution shown with a solid line corresponds to our optimal sample of 1089 DA stars with $S/N > 15$. In comparison, we show as a dashed line the distribution with an alternate cutoff of $S/N > 20$, scaled to match the former (the number of stars is given on the right-hand scale). The mean mass and standard deviation are given in the figure.

Fig. 8.— Comparison of spectroscopic and photometric temperatures (in % with respect to spectroscopic temperatures) as a function of spectroscopic temperature for all DA stars with $S/N > 20$ (open circles), excluding DA–M dwarf binaries. Blue filled circles correspond to double degenerate candidates discussed in the text, while red symbols represent outliers (2σ discrepancy) that have been flagged in Table 1 as problematic observations — see Notes

(1) or (2) in Table 1. The horizontal dotted line represents a perfect match between both temperature estimates.

Fig. 9.— Simulation of DA+DA (open circles) and DA+DB/DC (filled circles) binaries with synthetic models computed for every component combination in the range of $40,000 \text{ K} > T_{\text{eff}} > 6000 \text{ K}$ with steps of 2000 K. We studied the cases of two equal surface gravities ($\log g = 8$), and a difference of 0.5 dex ($\log g = 7.75, 8.25$). The resulting model spectra, with noise added, are fitted using the same procedure as that used to analyze the SDSS stars in Figure 8 (see text for more details). The smaller points correspond to simulations where the ratio in temperature between the hotter and cooler components is larger than a factor of two. The middle horizontal line represents the 1:1 relation, while the two other horizontal lines correspond to the 2σ region obtained from the SDSS distribution displayed in Figure 8.

Fig. 10.— Our best fits to the Balmer lines and He I lines, if present, for 35 double degenerate candidates in the SDSS sample. The lines are, from bottom to top, $H\alpha$ to H8, and He I $\lambda 5877$. Both the predicted and observed spectra have been binned by a factor of two for clarity. The atmospheric parameters, T_{eff} and $\log g$, of both H-rich and He-rich components are given in each panel; a value of $\log g = 8$ without decimals indicates that the value is assumed. The unexpected features in the core of $H\alpha$ for some objects (i.e., J040852.23–045504.7) are a common occurrence in the SDSS spectra, and the origin of these features is unknown to us.

Fig. 11.— Same as Figure 10.

Fig. 12.— Superposition of the predicted (blue dots) and observed (blue error bars) photometry for two objects taken from Figures 10 and 11 (and in Table 3). The atmospheric parameters obtained from our spectroscopic fits are used here to compute the predicted photometry; only the solid angle is adjusted. Both the observed (gray) and synthetic (red) absolute fluxes are then scaled to the r photometric band.

Fig. 13.— Top: our DA+DB solution for J015221.12–003037.3. The left panel shows our best spectroscopic fit reproduced from Figure 10, while the right panel shows the superposition of the observed and predicted photometry (only the scaling factor is adjusted here) using the same presentation format as previous figures. Bottom: our DAB homogeneous solution for the same object. The left panel shows our spectroscopic fit with an *assumed* helium abundance of $\text{He}/\text{H} = 10^{-2}$. Again, the right side represents a superposition of the observed and predicted photometry using the spectroscopic atmospheric parameters.

Fig. 14.— Same as Figure 10 for three objects but with an *assumed* hydrogen abundance of $\text{H}/\text{He} = 10^{-3}$ for the helium-rich components.

Fig. 15.— Left panels: our best fits to two DA stars with mixed H/He model atmospheres; a value of $\log g = 8$ is assumed in both cases. The atmospheric parameters are given in each panel. Both the predicted and observed spectra have been binned by a factor of two for clarity. Right panels: our best photometric fits for the same objects assuming a value of $\log g = 8$ and H/He abundances determined from the spectroscopic fits. Both the fluxed spectra (in gray) and synthetic model fluxes (in red), calculated at the spectroscopic parameters given in the left panel, are then scaled to the r photometric band.

Fig. 16.— Comparison of atmospheric parameters, T_{eff} and $\log g$, between our analysis and that of Eisenstein et al. (2006). The open circles represent DA–M dwarf binaries, while smaller symbols indicate spectra with $20 > \text{S/N} > 12$. We note that the model grid used by Eisenstein et al. is limited to $\log g < 9$, hence some of the discrepancies observed here result from this shortcoming.

Fig. 17.— Top panel: effective temperature differences (in %) for the 89 DA stars in common between the SDSS and Gianninas et al. samples. The observed spectra have been analyzed with the same models and fitting technique discussed in Section 2. The horizontal line represents a perfect match. Bottom panel: similar to the top panel but for differences in $\log g$ values.

Fig. 18.— Mass distributions as a function of T_{eff} for the SDSS sample (top panel) and the Gianninas et al. sample (bottom panel). Lines of constant mass at $0.55 M_{\odot}$ and $0.70 M_{\odot}$ are shown as a reference.

Fig. 19.— Top panel: mean mass of the SDSS sample for $T_{\text{eff}} < 13,000$ K computed in 1000 K temperature bins. The dotted line is the mean mass obtained from Figure 7 for hotter objects. Bottom panel: similar to the top panel but for the mass standard deviation.

Fig. 20.— Comparison of our T_{eff} and $\log g$ determinations with those of Silvestri et al. (2006) for the sample of DA–M dwarf binaries in the SDSS. The dashed line in each panel represents the 1:1 correspondence.

Fig. 21.— Same as Figure 7 but for the mass distribution of our sample of DA–M dwarf binaries with a DA component in the range $40,000 \text{ K} > T_{\text{eff}} > 13,000 \text{ K}$.

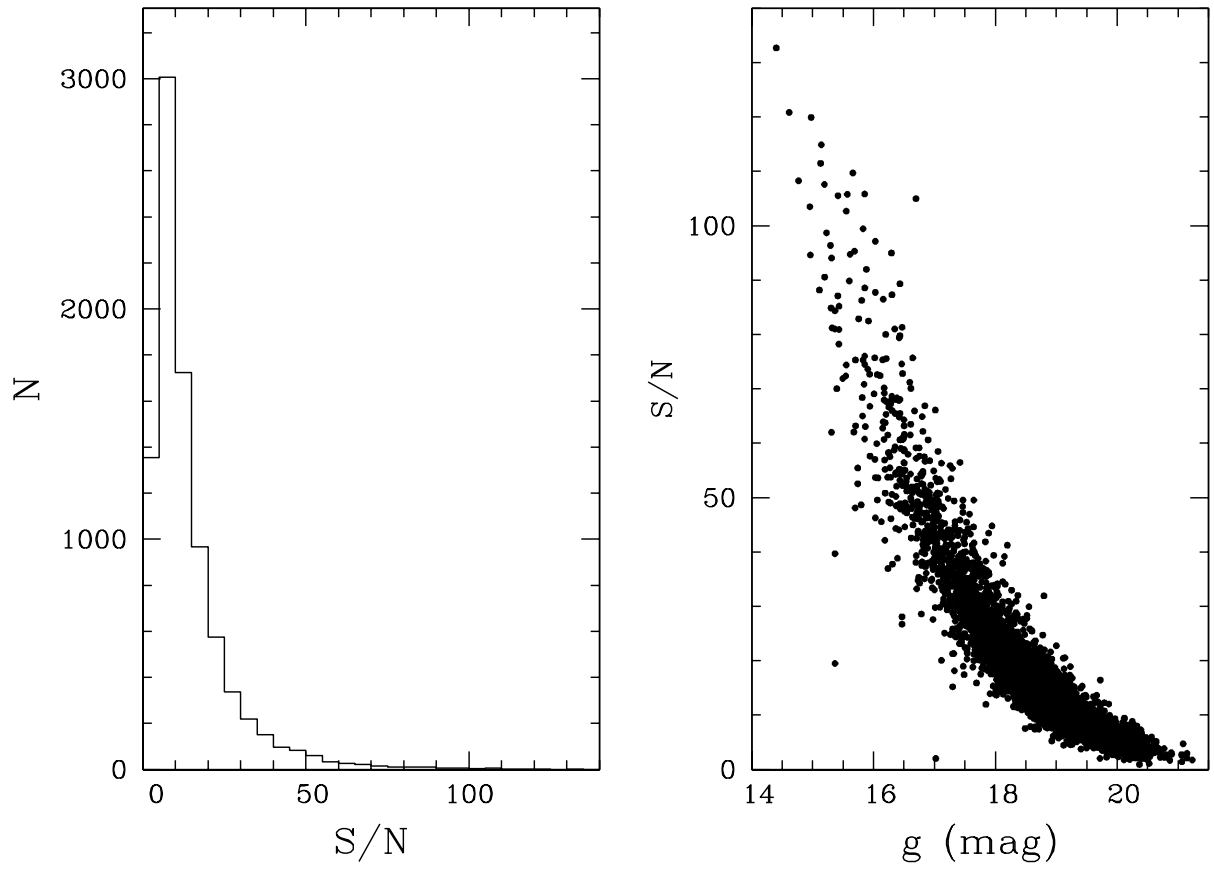


Figure 1

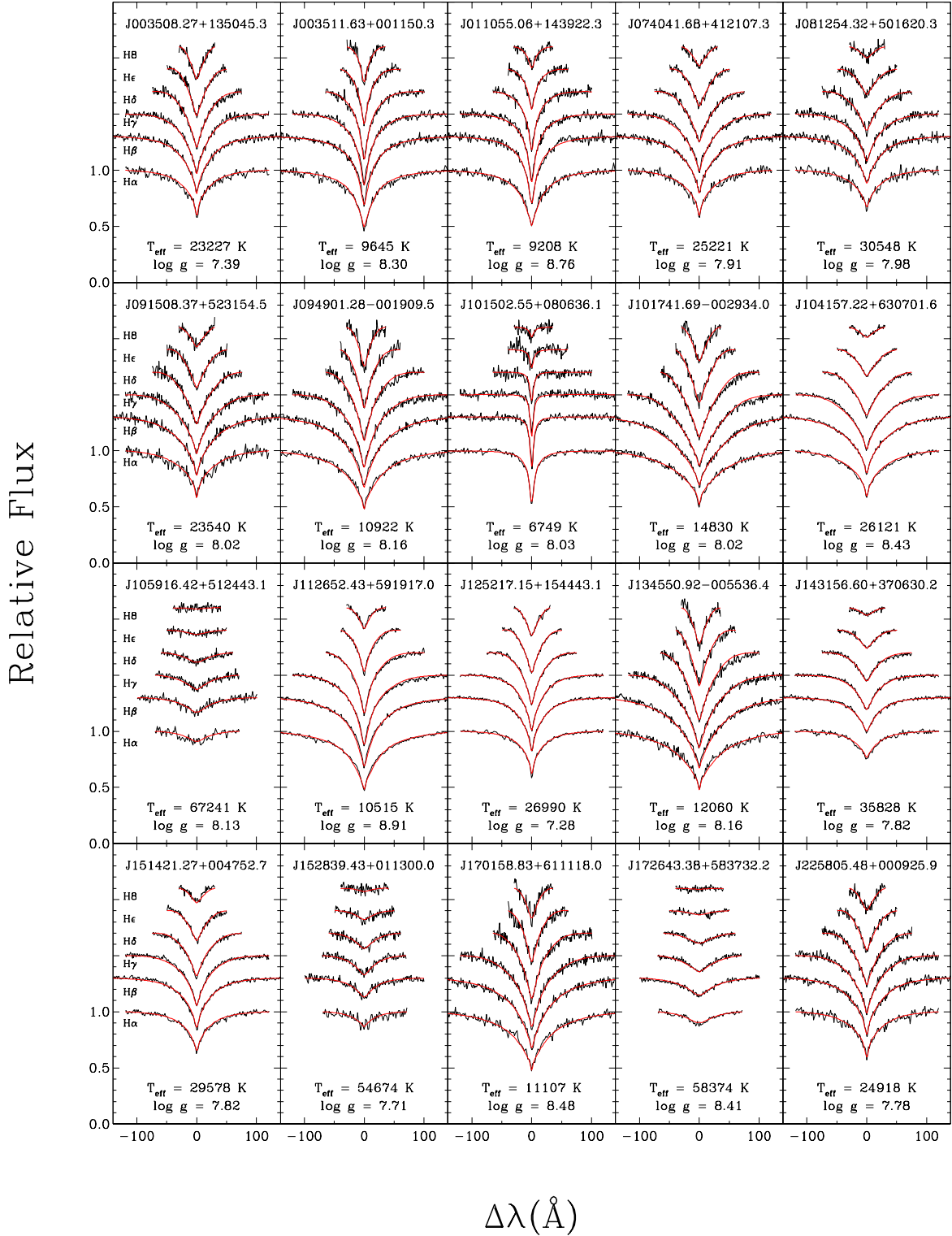


Figure 2

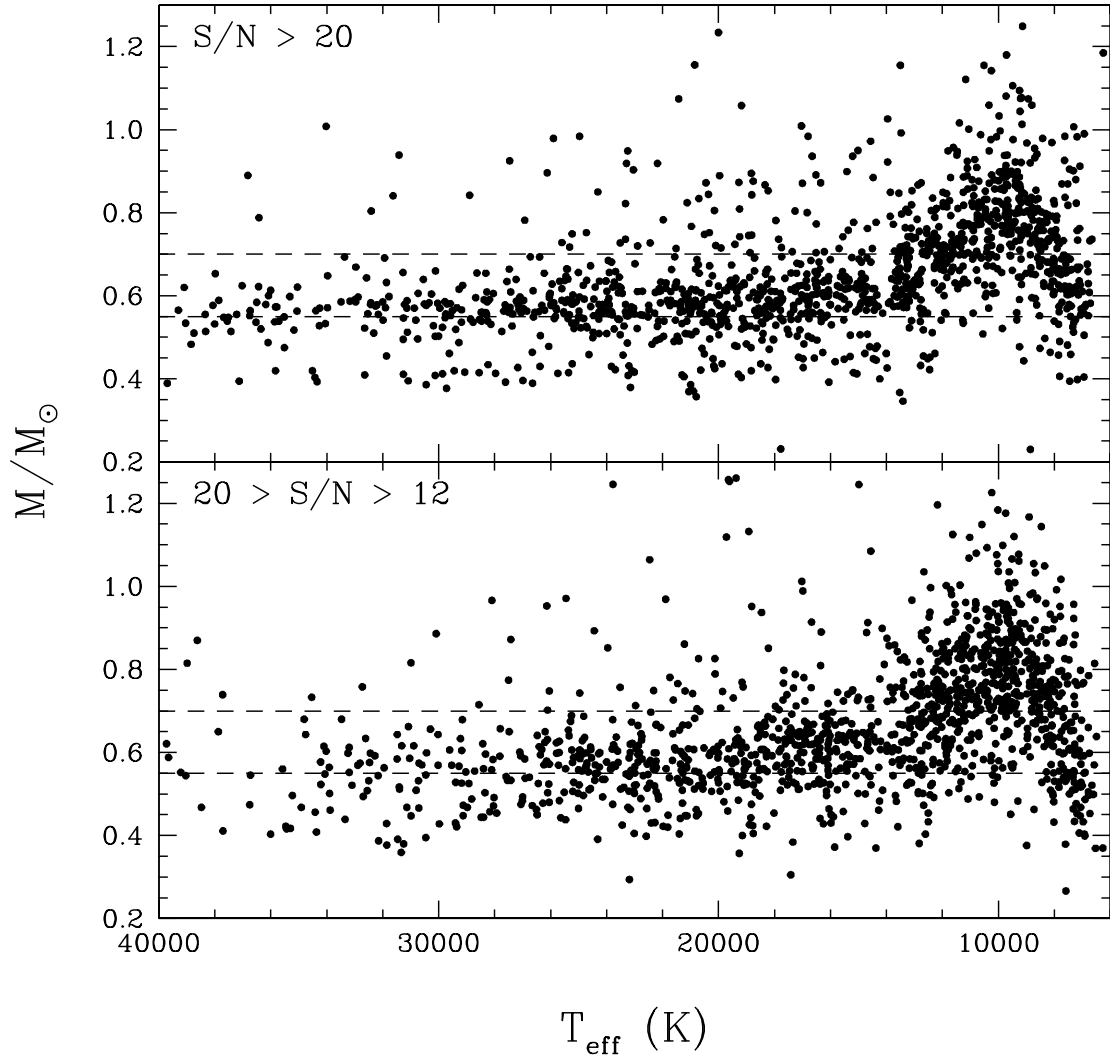


Figure 3

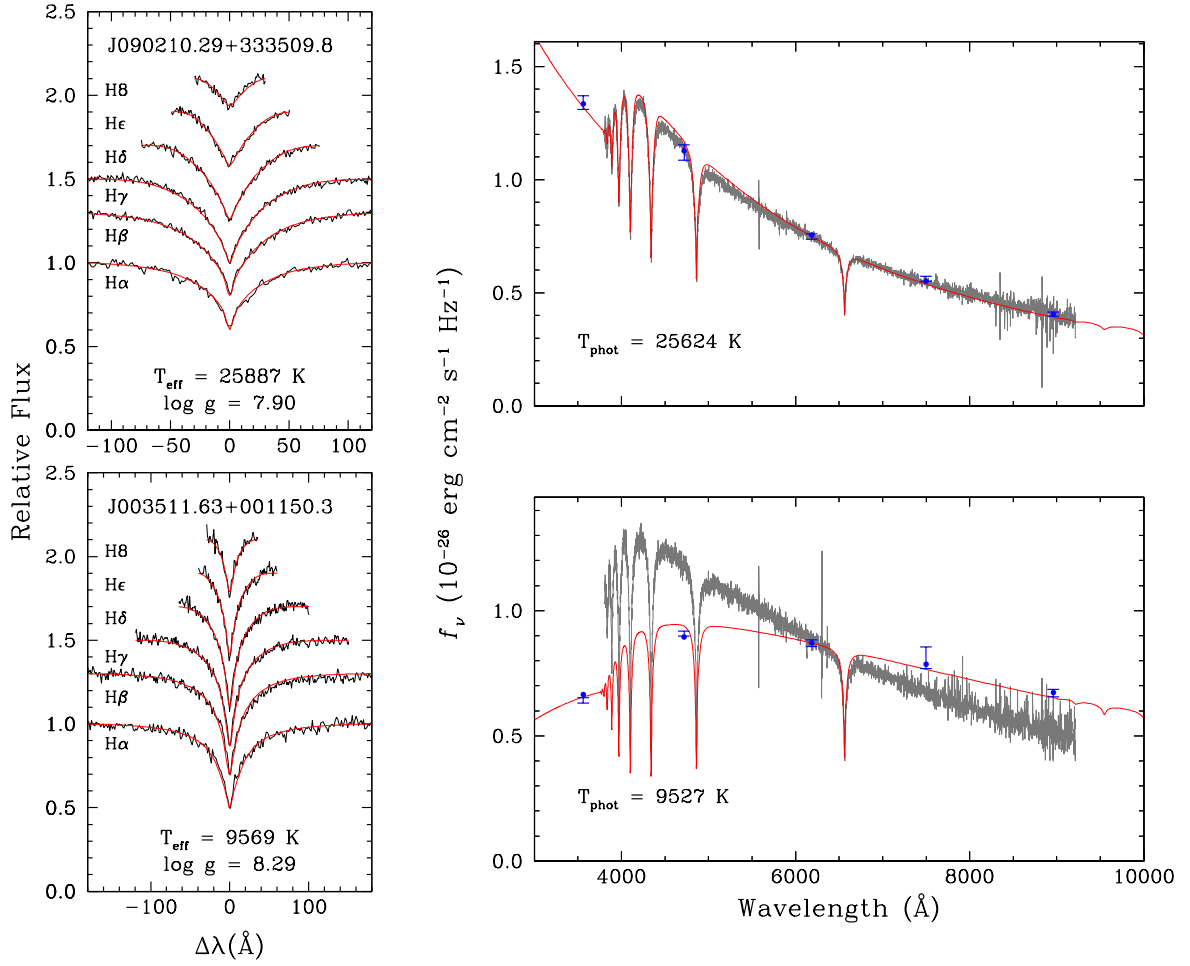


Figure 4

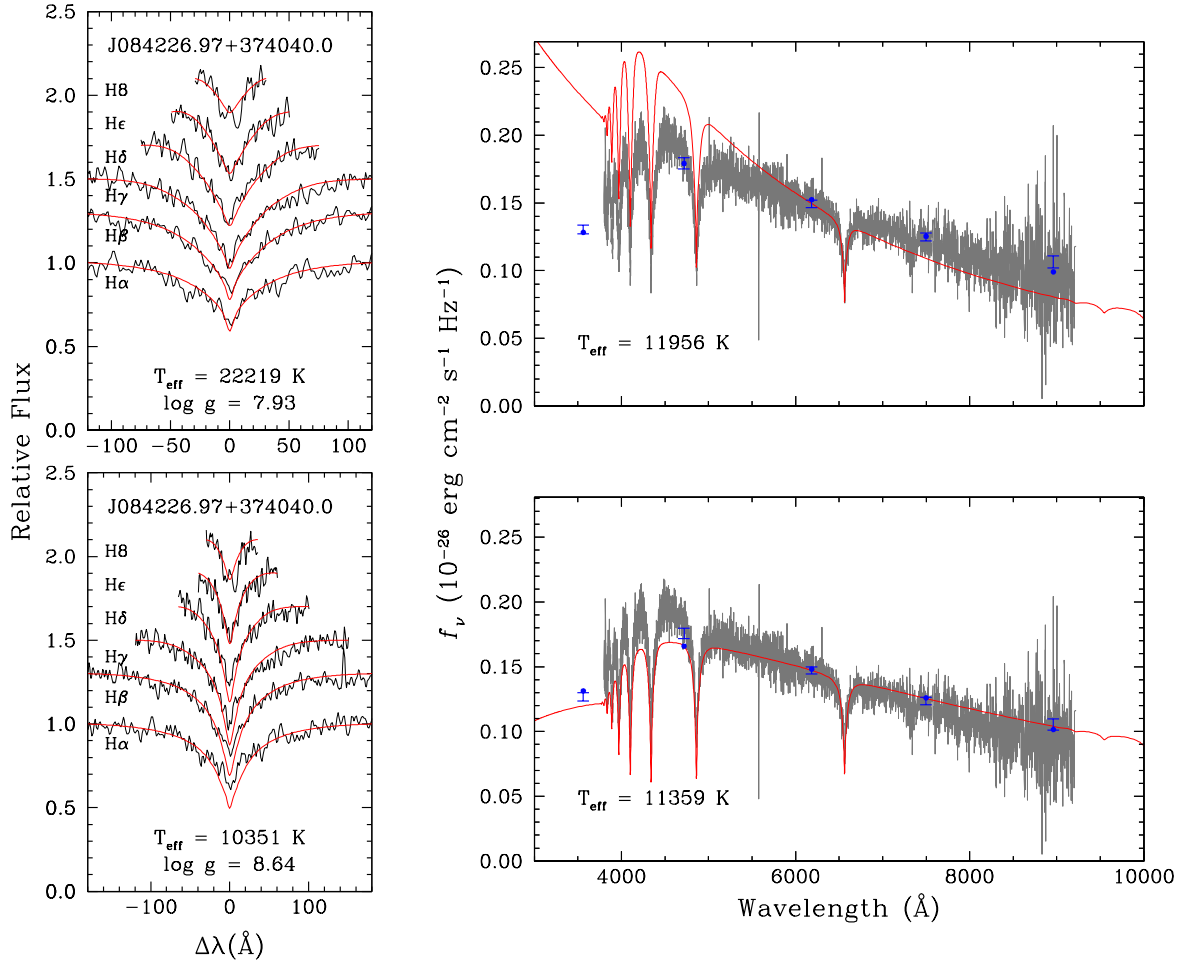


Figure 5

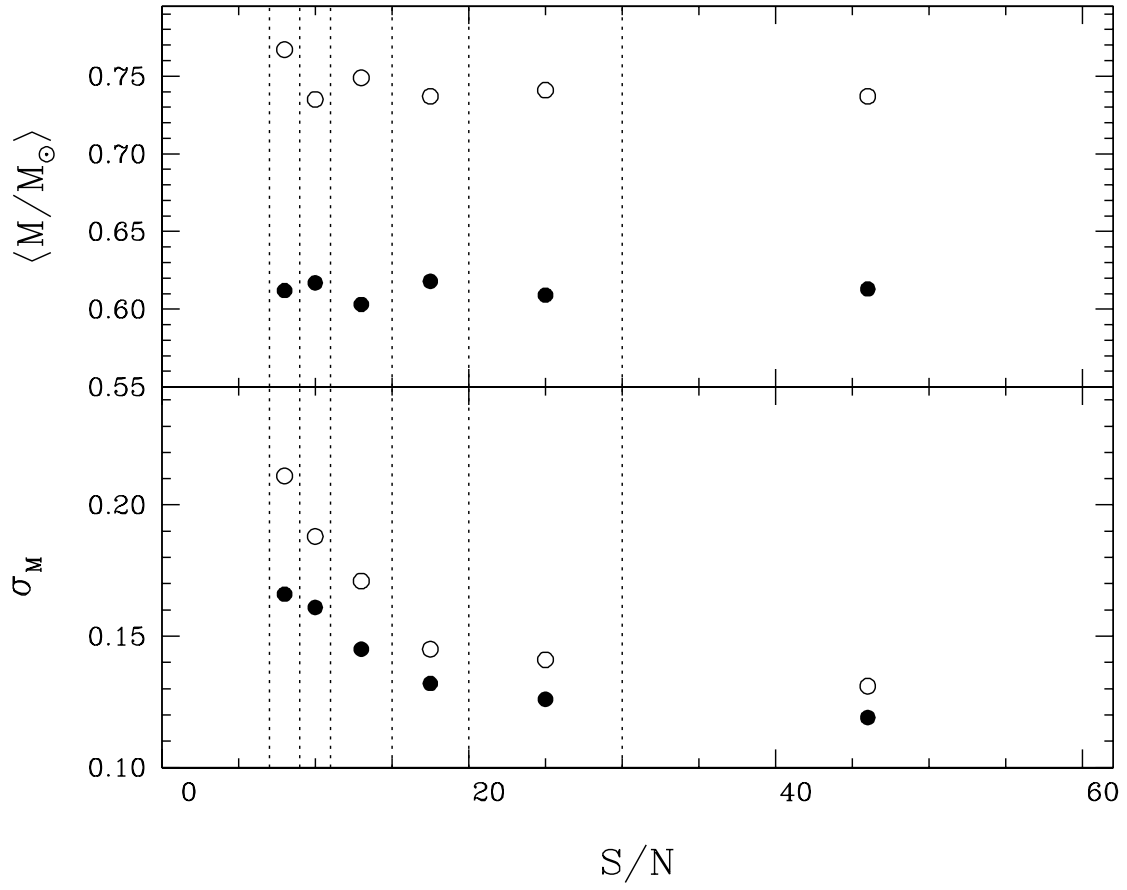


Figure 6

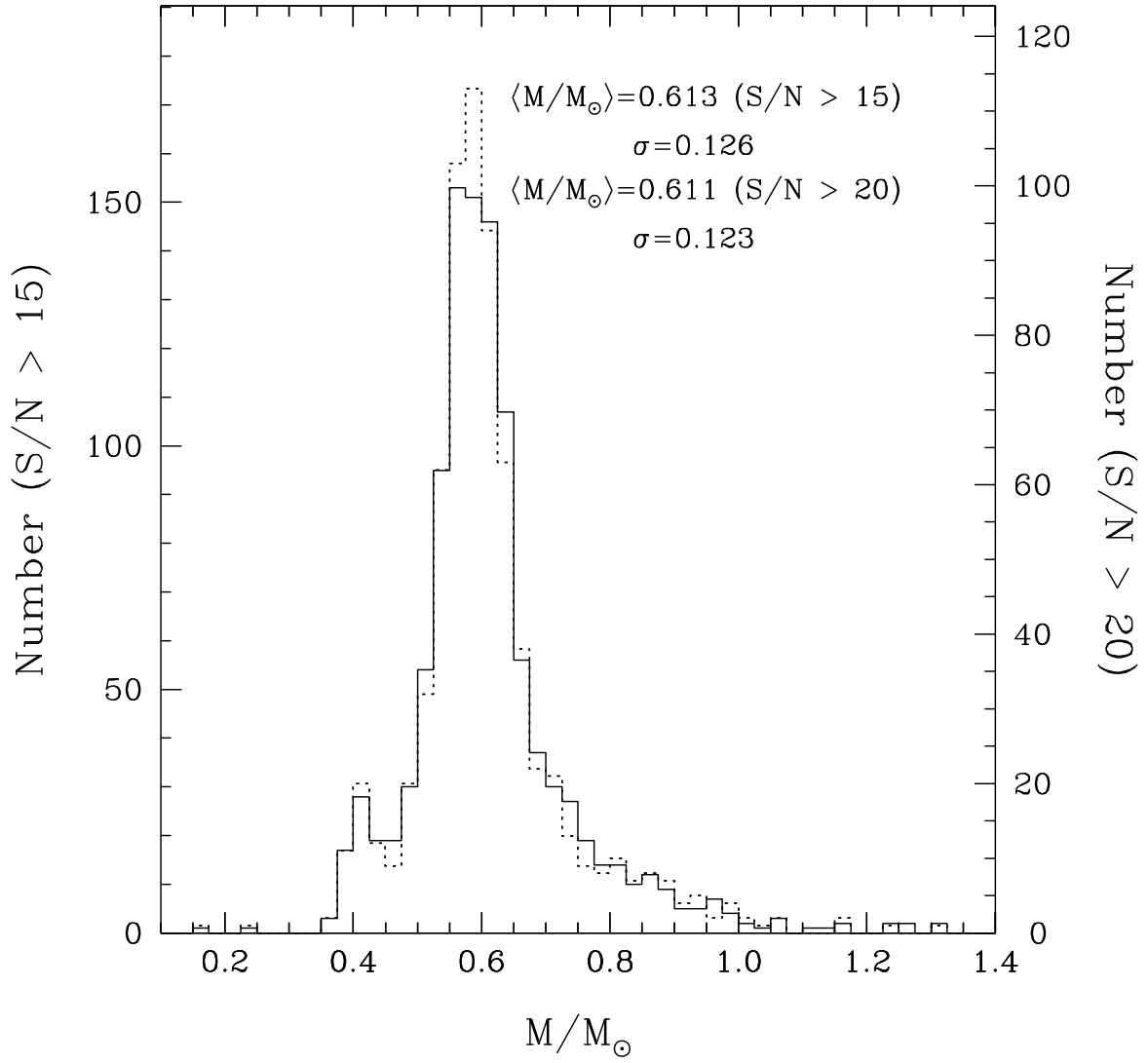


Figure 7

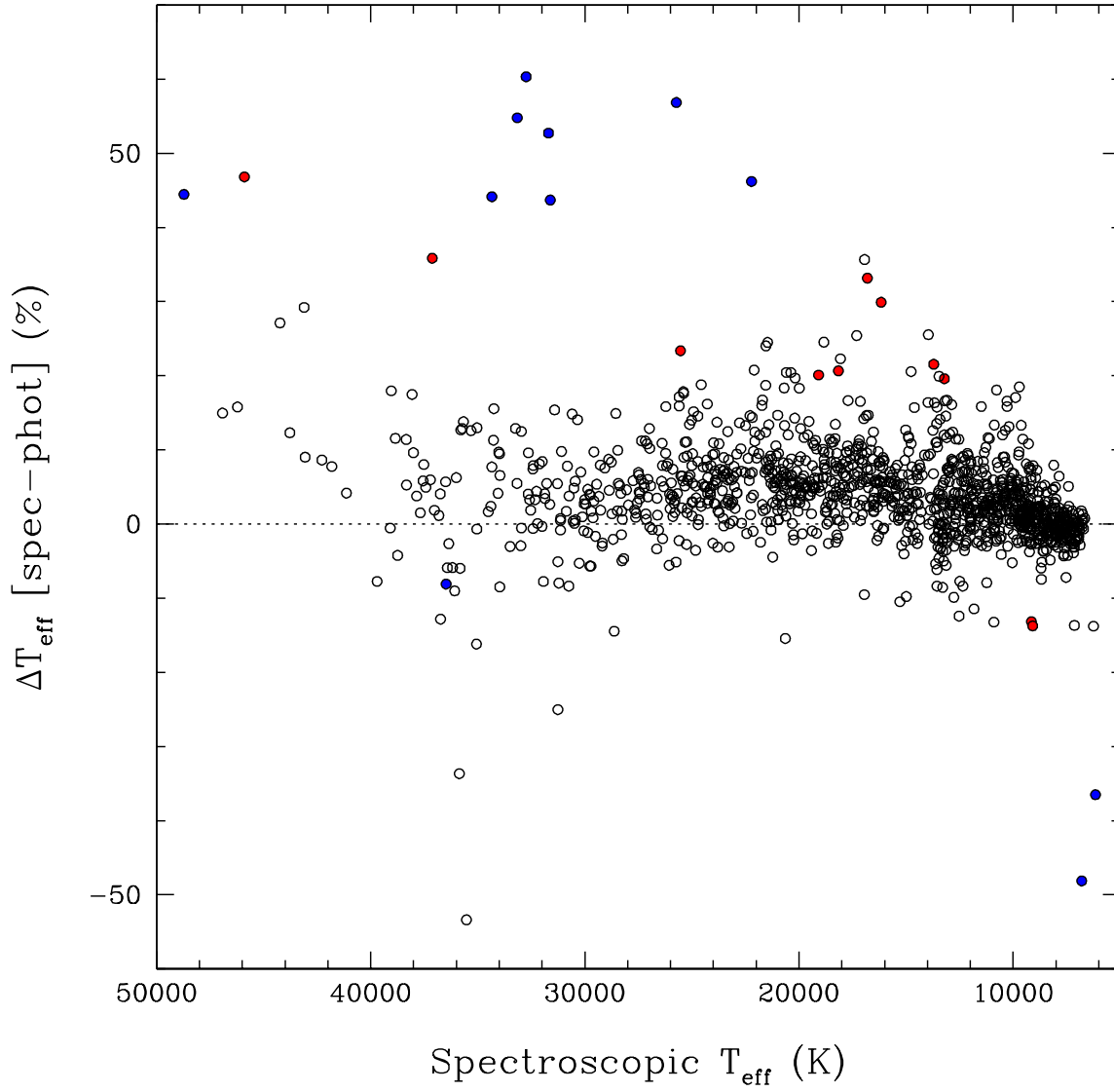


Figure 8

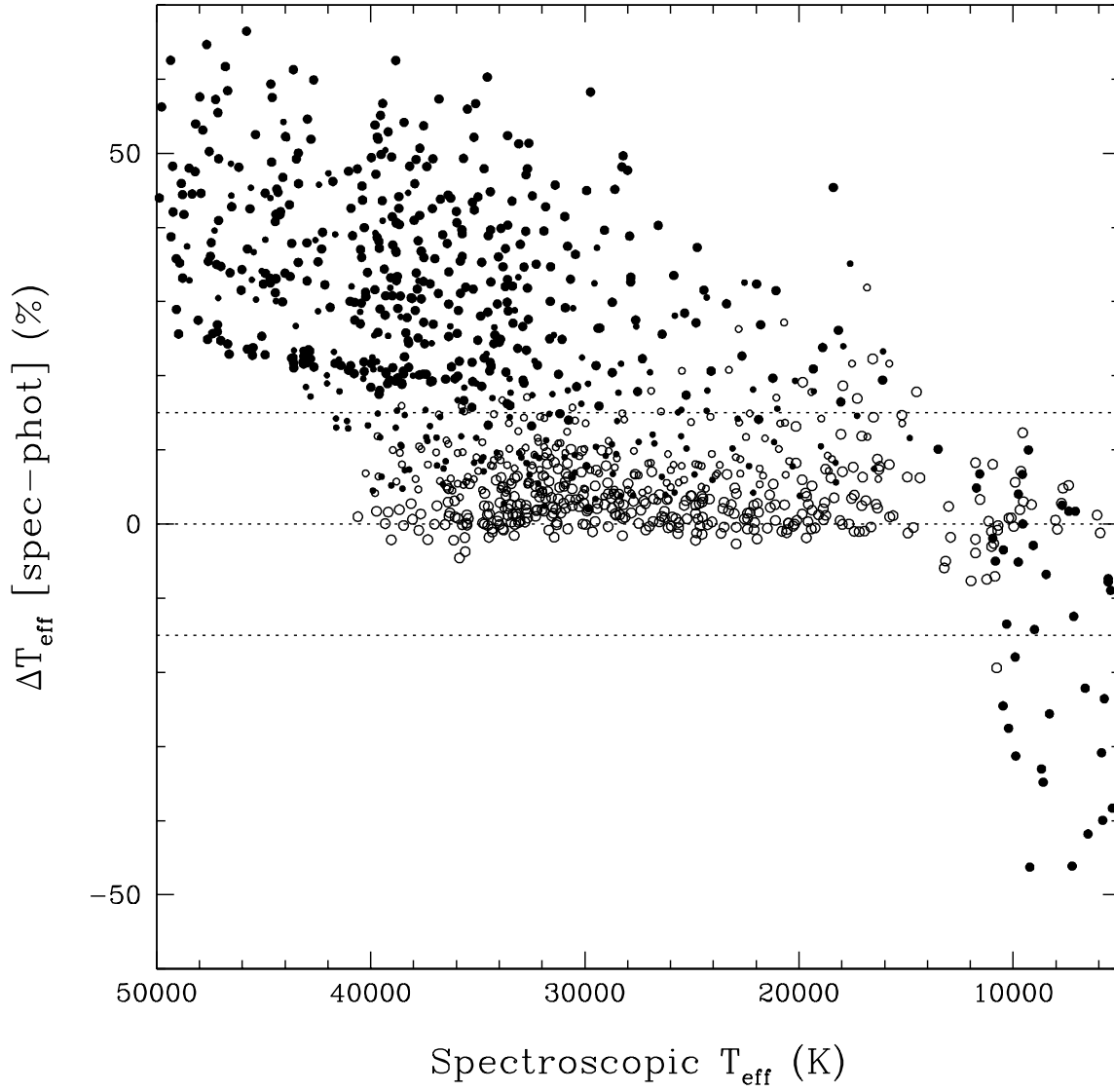


Figure 9

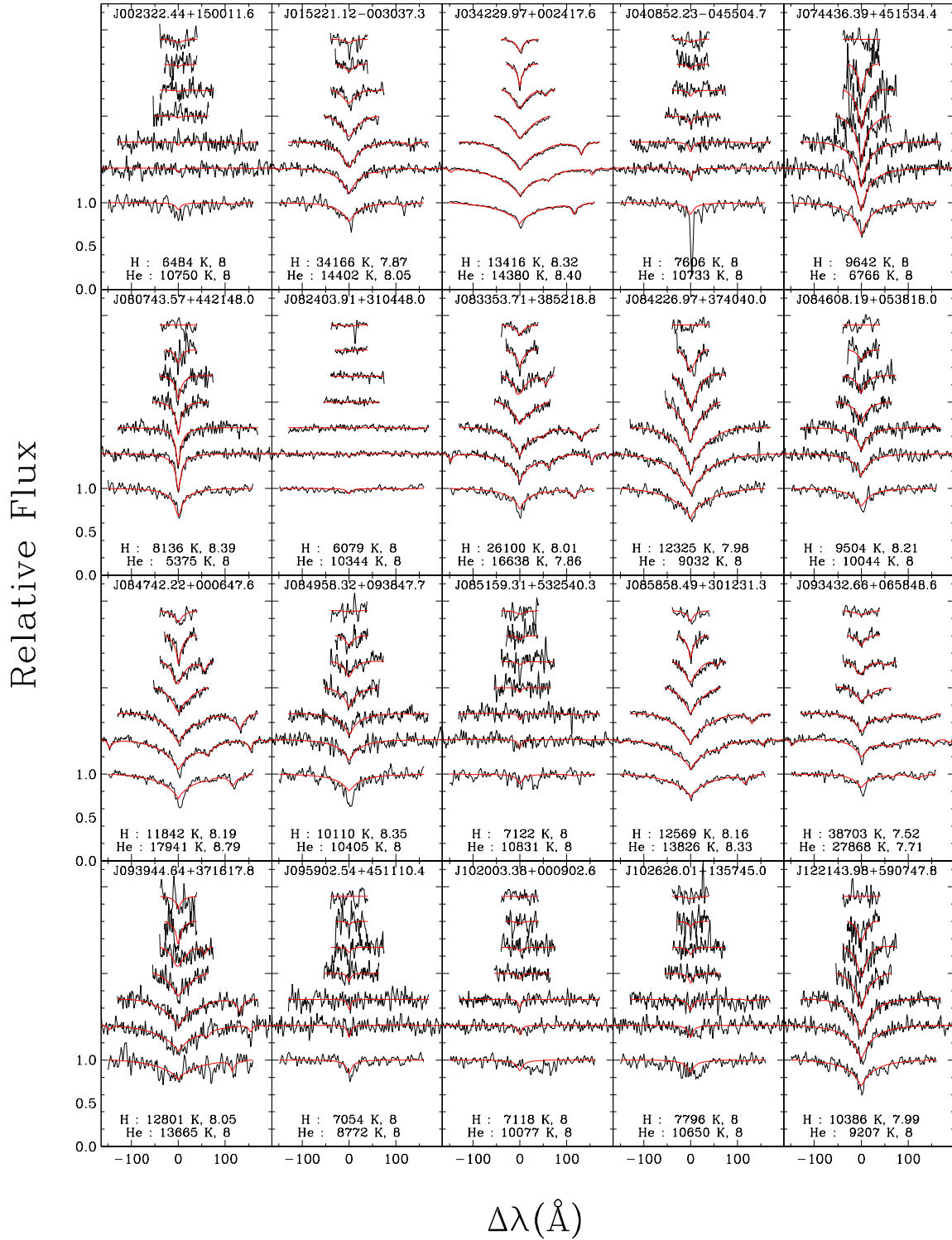


Figure 10

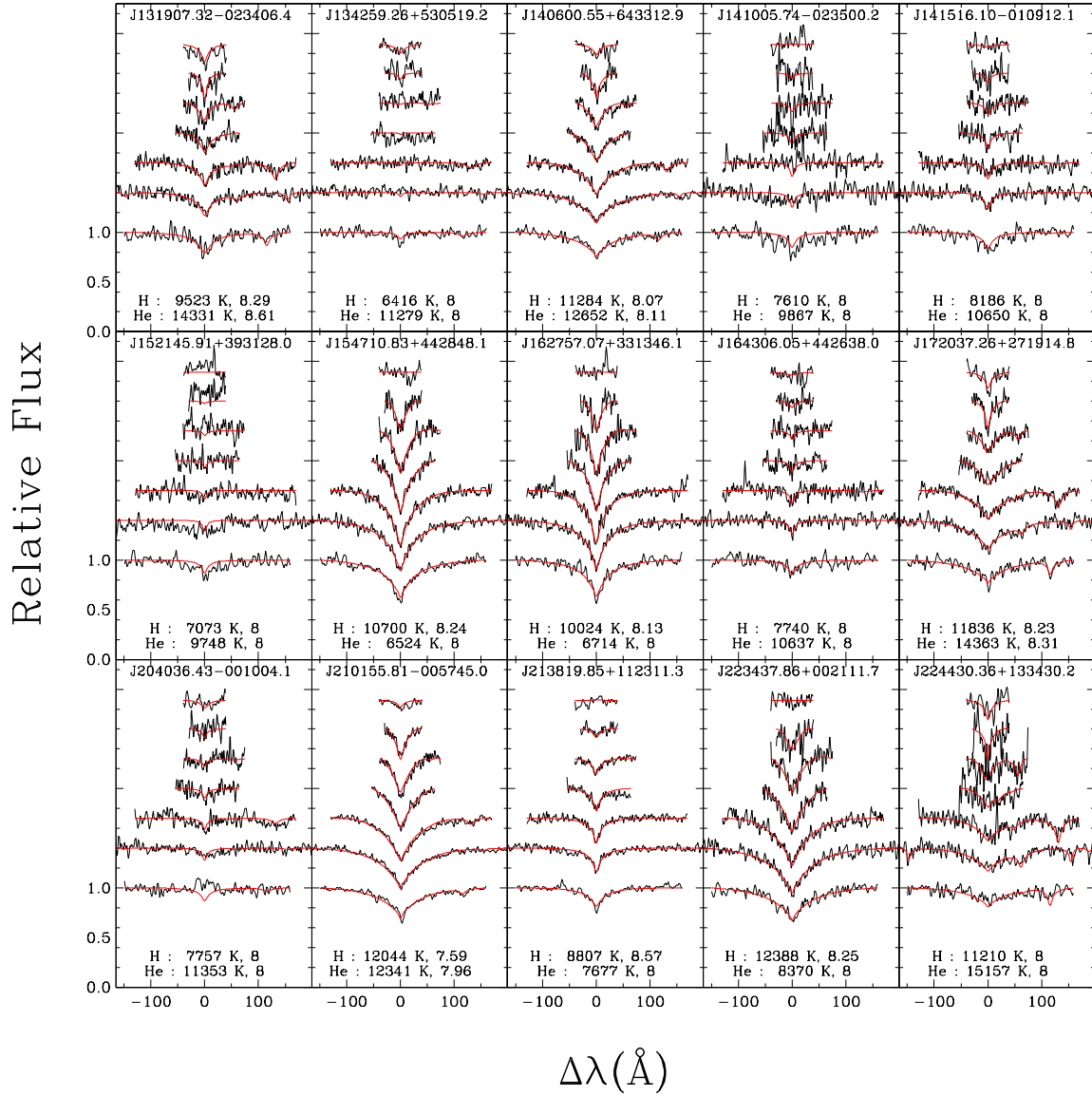


Figure 11

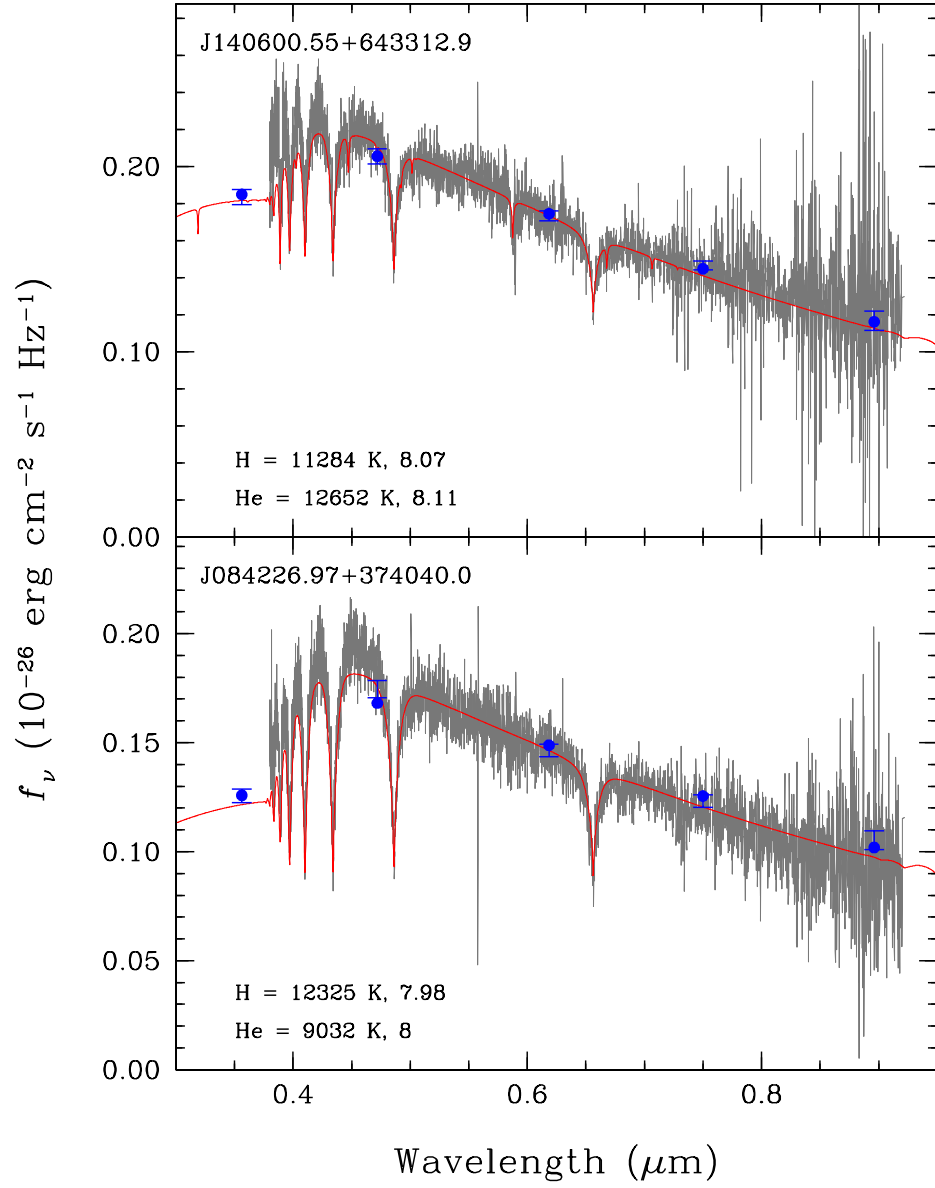


Figure 12

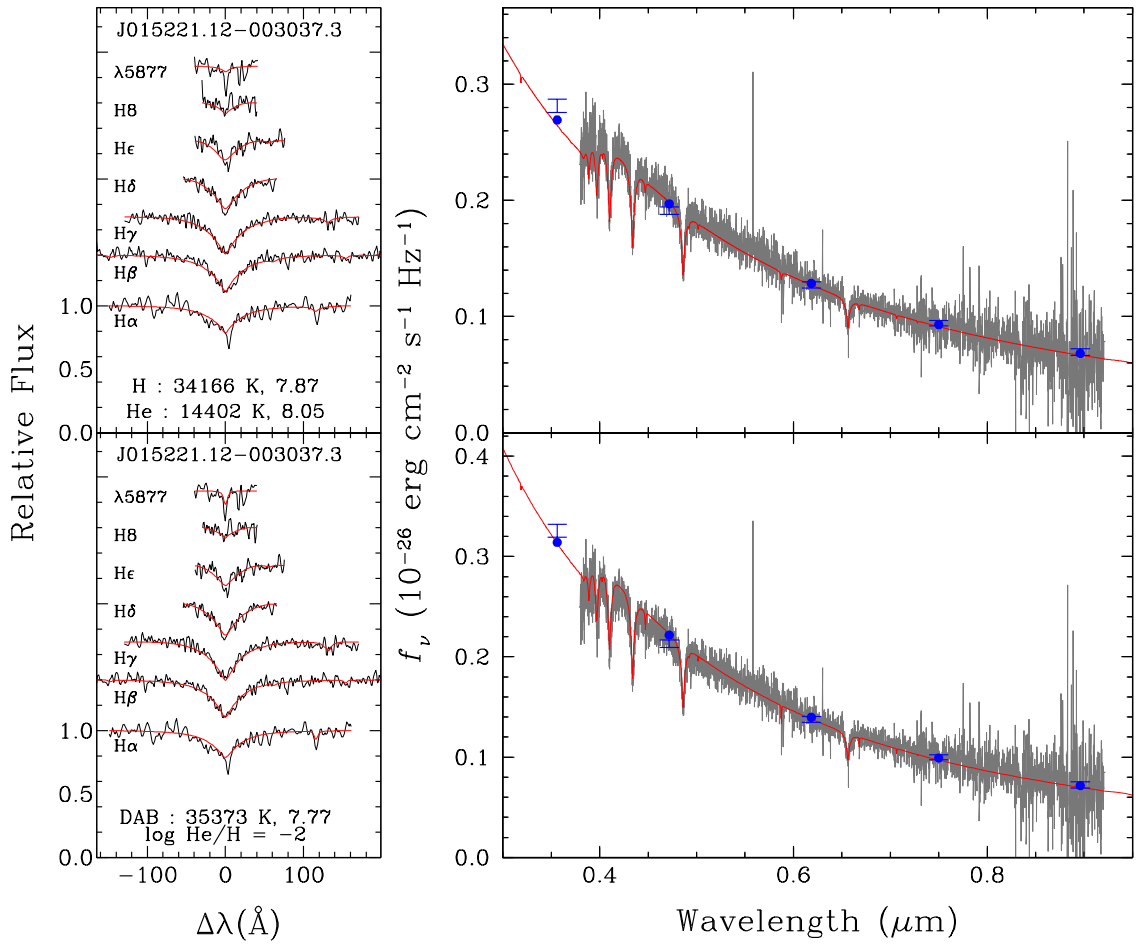


Figure 13

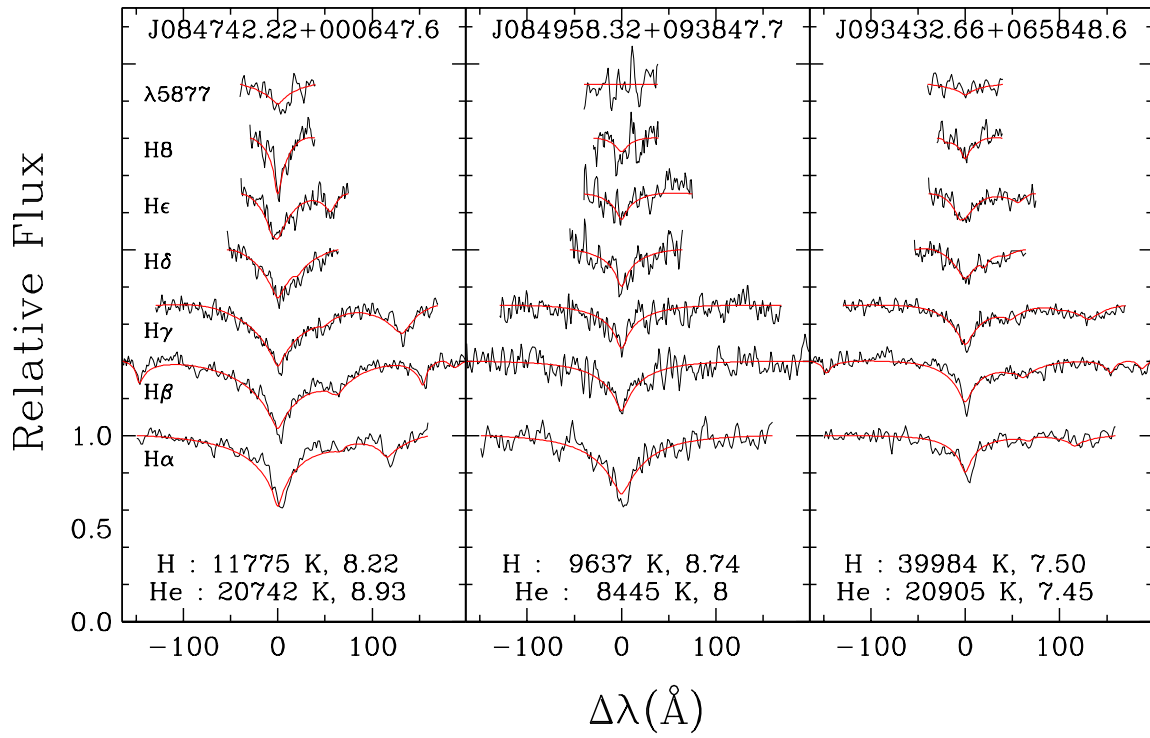


Figure 14

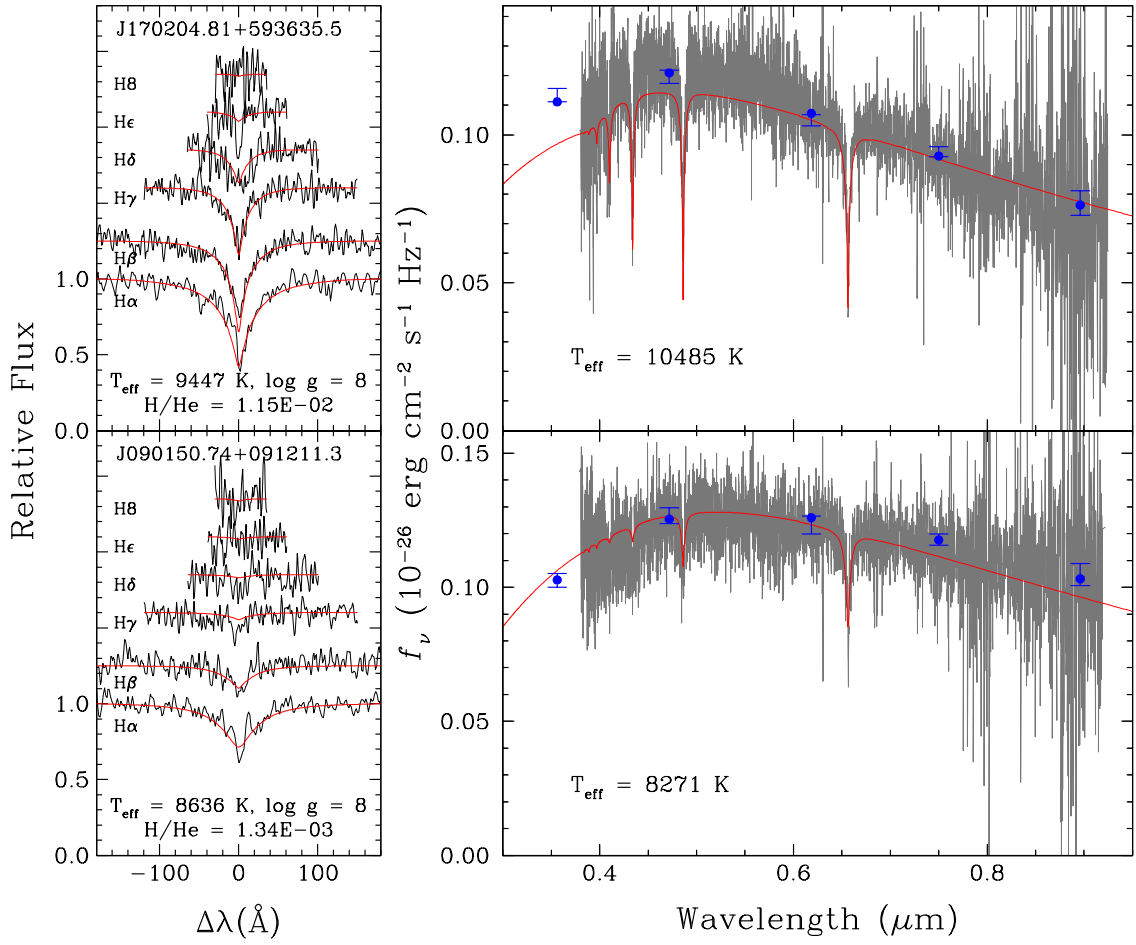


Figure 15

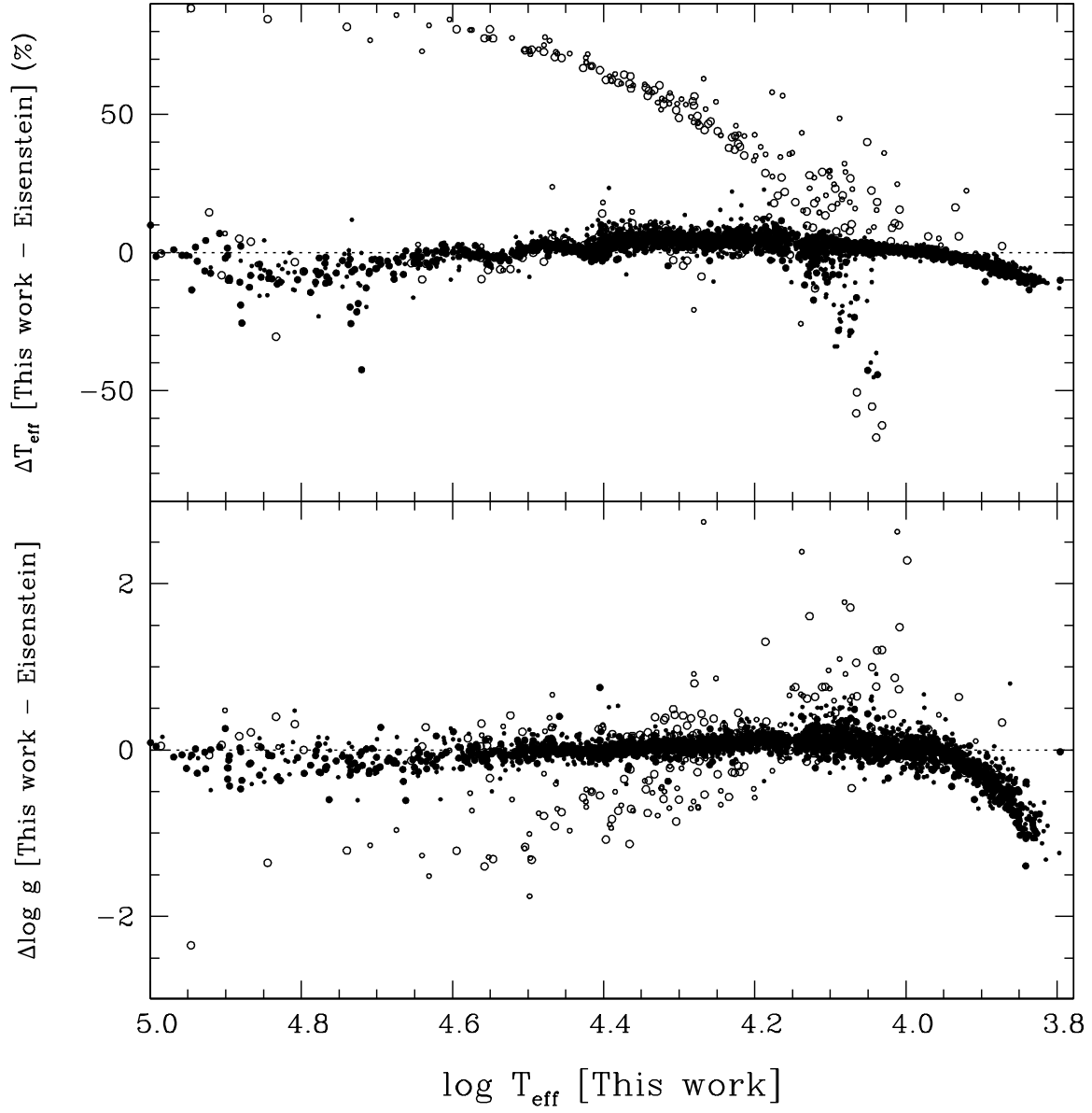


Figure 16

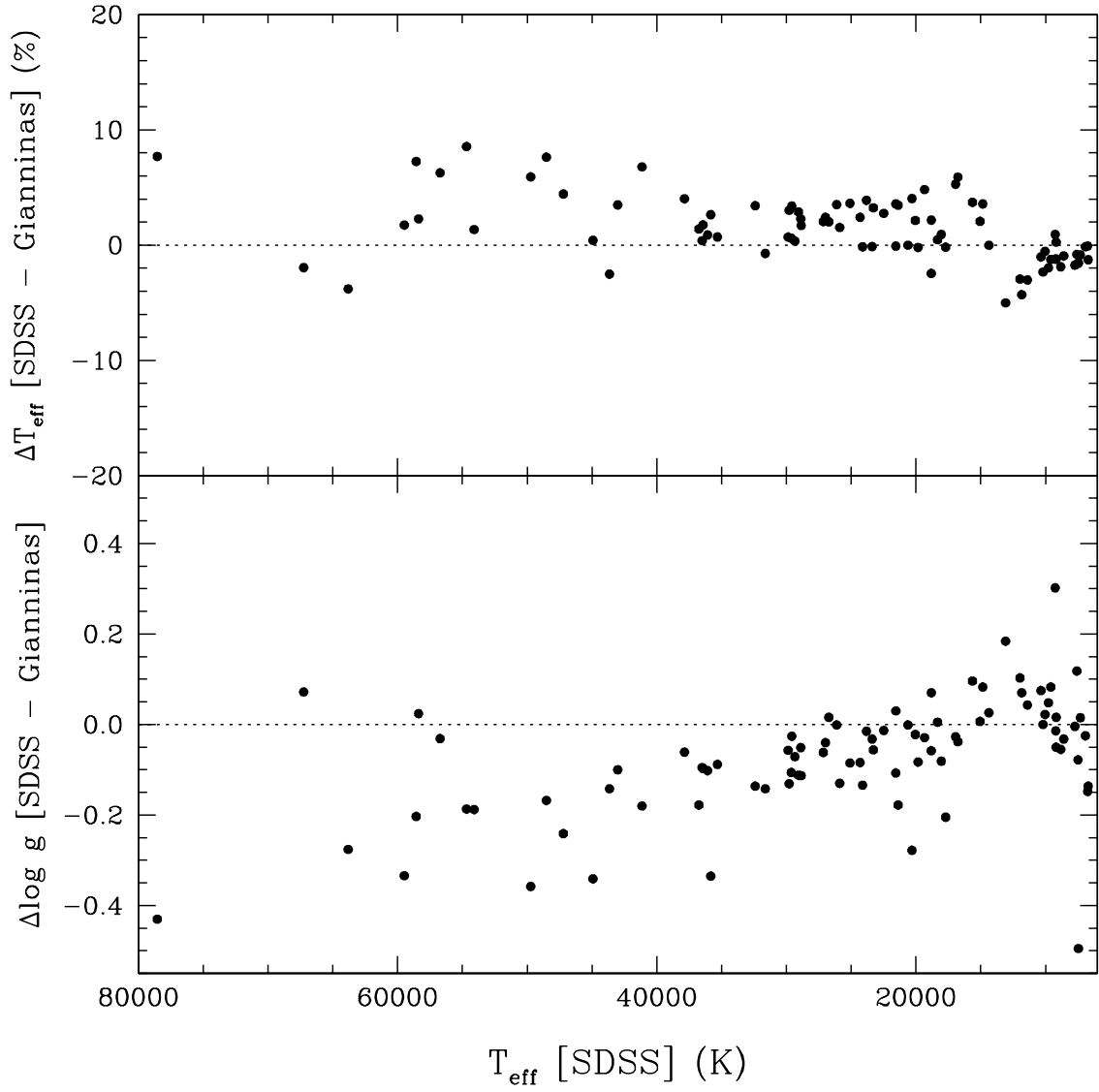


Figure 17

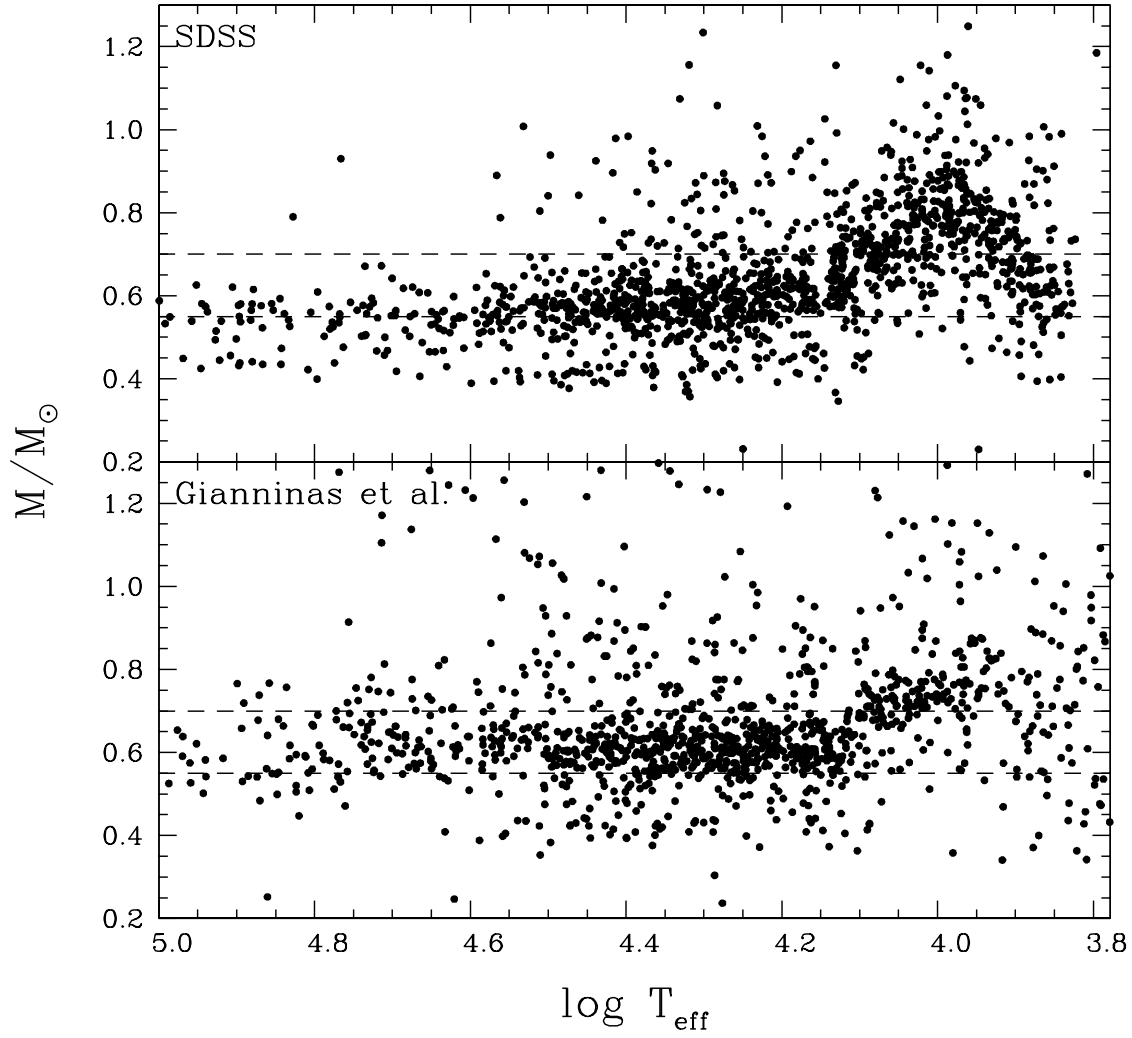


Figure 18

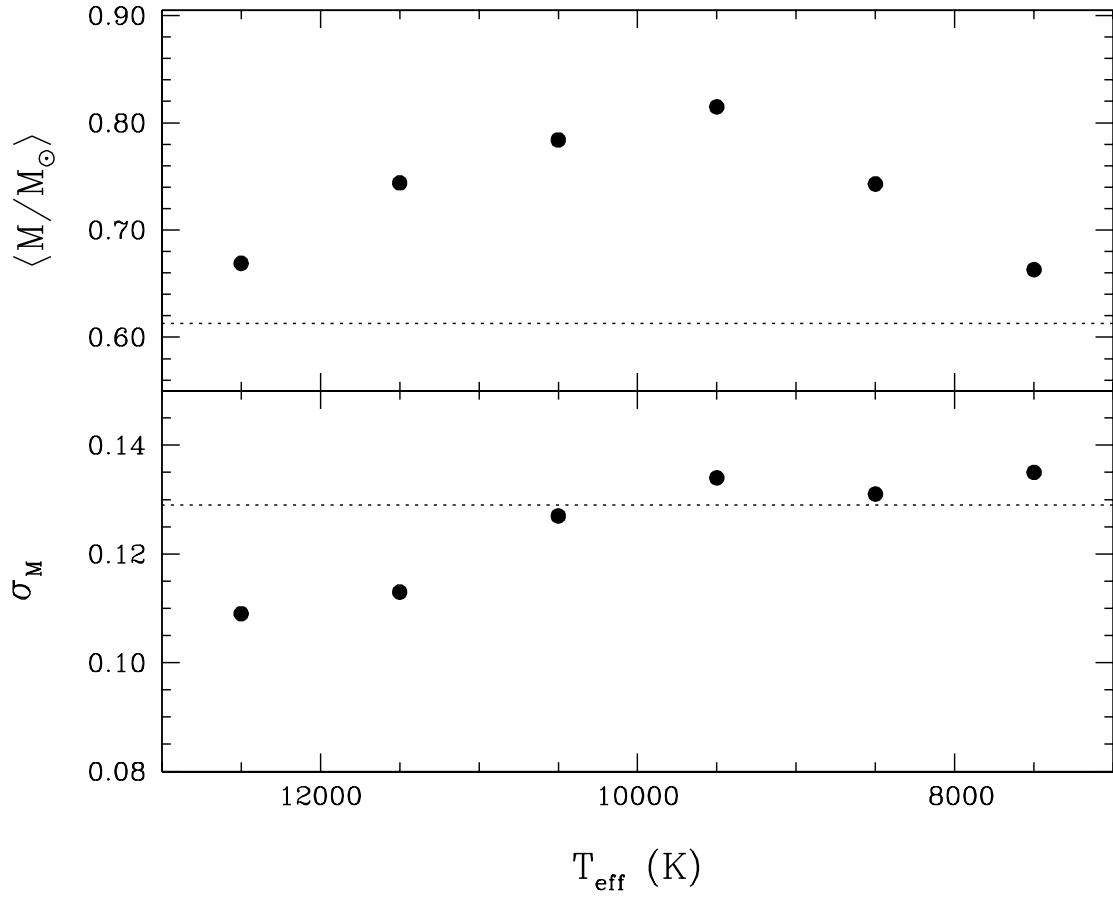


Figure 19

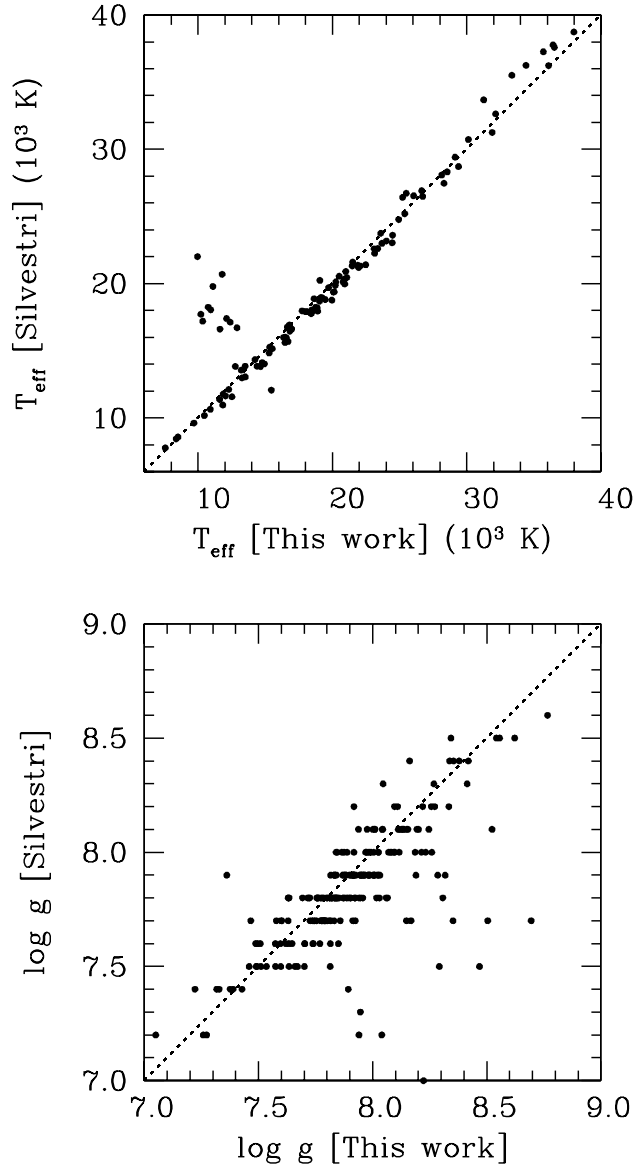


Figure 20

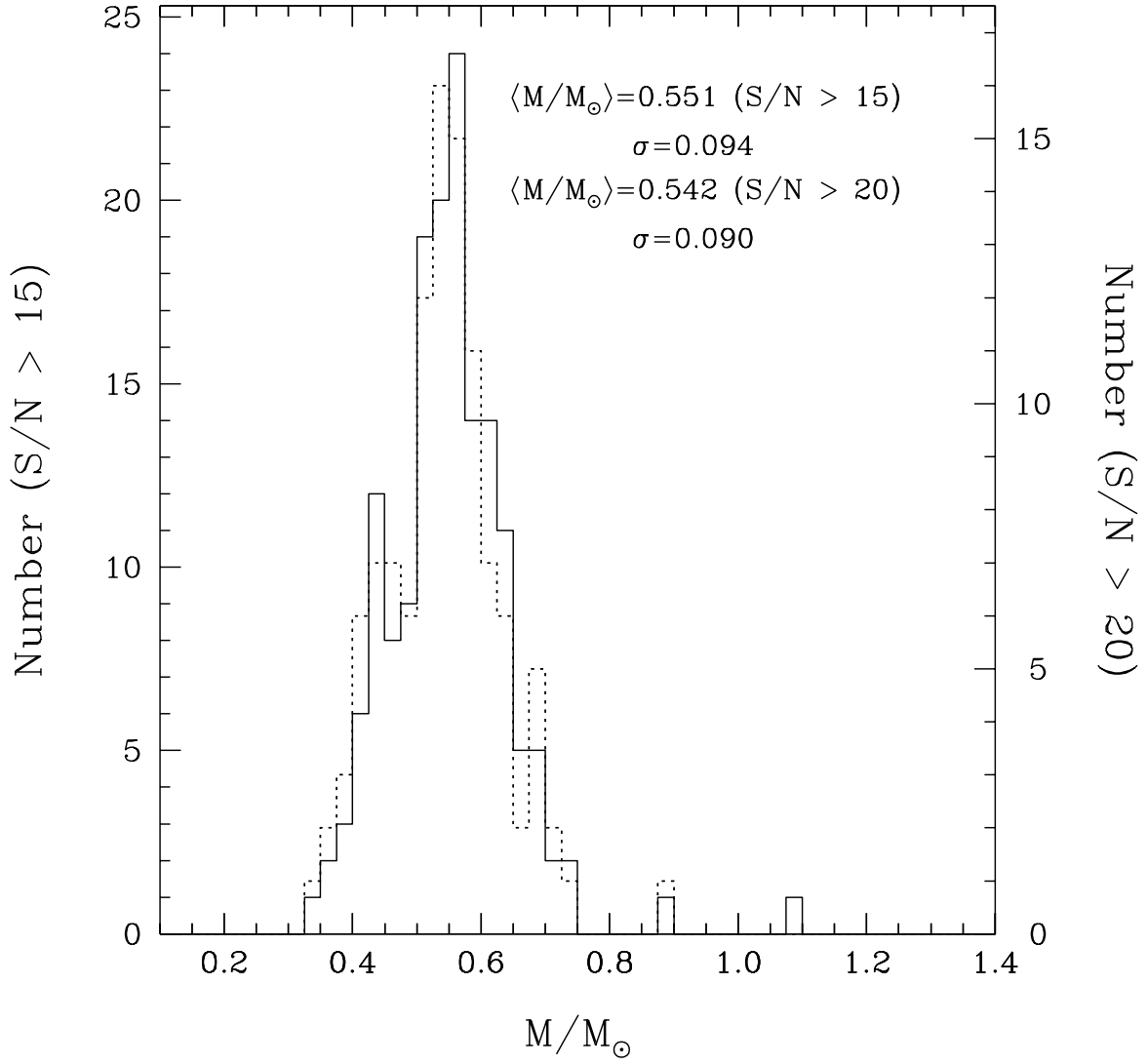


Figure 21